The Dissertation Committee for Jaeyoung Lim
certifies that this is the approved version of the following dissertation:

EXPERIMENTS ON DYNAMIC FRACTURE AND FRICTION

Committee:

K. Ravi-Chandar, Supervisor

Stelios Kyriakides

Kenneth M. Liechti

Eric B. Becker

Sikhanda S. Satapathy

EXPERIMENTS ON DYNAMIC FRACTURE AND FRICTION

by

Jaeyoung Lim, B.S.,M.S.

DISSERTATION

Presented to the Faculty of the Graduate School of
The University of Texas at Austin
in Partial Fulfillment
of the Requirements
for the Degree of

DOCTOR OF PHILOSOPHY

THE UNIVERSITY OF TEXAS AT AUSTIN
December 2007

Dedicated to

my wife *Sunmyung Kim* and daughter *Kate Miru Lim*.

Acknowledgments

It was a great experience for me to spend my life in Austin during my Ph.D. studies. I met many good people and learned a lot from colleagues and professors.

First of all, I would like to sincerely thank Dr. K. Ravi-Chandar for his support and guidance during my Ph.D. studies. I also would like to thank my other four committee members for their helpful suggestions and discussions of this dissertation: Dr. S. Kyriakides, Dr. Kenneth M. Liechti, Dr. Eric B. Becker and Dr. Sikhanda S. Satapathy. I am very grateful to my colleagues in our Laboratory: Dr. Haitao Zhang, Dr. Yong Zhu, Bisen Lin and other colleagues.

I am also very grateful to Korean colleagues in Department of Aerospace Engineering and Engineering Mechanics. Especially, I am grateful to the former Ph.D. students: Dr. Mintae Kim, Dr. Soojae Park, Dr. Changwan Kim and Dr. Kilho Eom for their encouragements and support. I am also grateful to current Ph.D. student: Se-hyuk Im, Minkyoo Kang, Dochul Yang and other colleagues.

Finally, I would like to thank all my family in Korea. Especially, I am deeply grateful to my parents and parents-in-law for their support, encouragement and prayers. I am also indebted to thank my family in Austin, especially, my wife for her endless support, love and trust when I was in trouble. My daughter, Miru gave me a powerful energy which made progress in my research possible.

Jaeyoung Lim

The University of Texas at Austin
December 2007

EXPERIMENTS ON DYNAMIC FRACTURE AND FRICTION

Publication No. ____________________

Jaeyoung Lim, Ph.D.
The University of Texas at Austin, 2007

Supervisor: K. Ravi-Chandar

Dynamic fracture and friction under dynamic loading conditions are examined through direct observations in carefully controlled experiments. An electromagnetic loading device is used to generate a compressive stress wave and the full-field optical technique of dynamic photoelasticity and high-speed photography are used as diagnostic tools. In addition, a new optical method to determine both principal stresses and their orientations simultaneously is developed. In this dissertation, the results from experiments aimed at investigating fracture and frictional sliding under shear loading conditions are presented.

For dynamic fracture problems, we examine shear cracks in homogeneous materials by introducing a groove in the specimen and trapping the crack to grow within it. The groove does not affect the fracture mechanisms

inherent to the material, but influences the energy flux and loading symmetry. Such shear induced cracks growing at speeds in the intersonic regime are demonstrated. Furthermore, it is shown that the main mechanism of the shear crack growth is the sequential nucleation, growth and coalescence of echelon cracks. The spacing and angle relative to the groove plane of the echelon cracks are measured directly from the experimental specimen. Numerical simulation shows that the echelon cracks are well aligned perpendicular the maximum principal (tensile) stress generated in this specimen. The spacing is interpreted as an intrinsic characteristic of the failure process. These experiments also enable the determination of the dynamic failure stress at which microcracks are nucleated.

For frictional sliding along an interface, a novel apparatus has been constructed for the understanding of the nature of dynamic friction and studying the slip pulse propagation under extremely high rates of loading. In experiments, dynamic slip along the frictional interface are triggered either by a compressional planar wave, or a compressional cylindrical wave. In both methods, the stress state across a frictional interface is brought to the critical state behind the wave. When slip occurs across the interface, it is forced to run along the interface at the speed of this wave. Several interesting results on frictional sliding are presented. First, the stress drop across the slip interface is characterized from isochromatic fringe patterns. Evaluation of the fringe pattern yields a description of the evolution of the shear stress both ahead and behind the slip event. The shear stress is seen to build up gradually to a

maximum at the leading edge of a slip pulse and to decay rapidly over a few mm slip length. Second, slip pulses can be generated from frictional interfaces through interaction with propagating stress waves and are observed to propagate at a speed controlled by the wave that generates slip. Accumulation of fringes near the slip pulse and the orientation of the Mach lines suggestion the slip pulse propagates at a speed close to the dilatational wave speed.

Finally, new optical method in which the classical methods of photoelasticity and Mach-Zehnder interferometry are used in a combined arrangement is presented. In dynamic problems the measurement is made with a high-speed photodetector at very high temporal resolution at a single point or a small array depending on the detector array and recording device; this eliminates the need for a high-speed photographic system, but more importantly provides complete, time-resolved evolution of all stress components. Examples of application of the method are demonstrated.

Table of Contents

List of Tables

List of Figures

Chapter 1

Introduction

1.1 Dynamic Fracture under Mode II Loading

Dynamic fracture problems in solids have studied intensively for nearly five decades. Much of this work has been aimed at cracks growing under opening mode or mode I type of loading. This is primarily due to the fact that crack growth in homogeneous materials is seldom observed under locally shear dominant conditions; in fact, this observation is the basis for the postulate of the *criterion of local symmetry* typically used in the determination of crack paths under mixed-mode loading even under quasi-static conditions. The reasons for preferring the locally opening mode of crack growth are rooted in the energetics of fracture: the energy required to grow a crack along the direction of local tension is smaller than the energy required to drive the crack under local shear. However, problems in interfacial fracture, earthquake mechanics and high speed sliding, where the crack is forced to grow under mode II conditions have sparked an interest in mixed-mode or pure mode II loading conditions.

While there have been many experiments where shear fracture was observed - for example, von Karman [57] performed experiments under confinement and produced graphic examples of shear fracture - it is still difficult to determine the fracture energy or toughness for crack growth under pure mode II conditions; there have been very few attempts to measure this quantity experimentally. Note that we do not consider the evaluation of the critical mode II loading at which a favorably oriented opening mode crack initiates and grows as a characterization of the shear fracture toughness; this is not the fracture energy for a shear crack. Notwithstanding the experimental difficulties, some attempts have been made to measure the shear fracture energy. Wong [61] performed shear crack experiments in rocks and found that the critical energy release rate for shear cracks is at least two orders of magnitude larger than that for tensile cracks! Broberg [7] constructed an ingenious apparatus to examine shear crack growth. By performing an experiment in polymethylmethacrylate (PMMA) under biaxial compression, a crack was observed to grow along the plane of maximum shear. A crack at an angle of 54° was introduced into an 83 mm x 83mm square plate and subjected to uniaxial and biaxial compression. Under uniaxial compression, a kinked, wing crack grew as a mode I crack while under a critical biaxial compression, a straight mode II crack was grown. Broberg determined that the mode II fracture toughness was about 2.5 times the mode I fracture toughness. This difference in the energy requirements between the opening mode and shear mode of fracture accounts for the fact that in experiments where biaxial confinement is not present, the crack growth is dictated by the lower energy mode I path and hence the validity of the criterion of local symmetry for homogeneous media.

Growth of mode II cracks is easier to envision in heterogeneous media, layered structures or at interfaces. Examples of these would include single crystals, composites, bonded joints, faults on the earth's crust etc. Here the fracture plane heterogeneity or weak interface provides for a variation in the fracture energy, thus guiding a shear mode crack to grow along an interface; such cracks may grow quasi-statically or dynamically. Under quasi-static loading conditions, Liechti and Chai [32] performed careful characterization of crack growth in bimaterial interfaces, and with the help of local measurements of the displacement field, determined that the fracture energy depended significantly on the ratio of opening to sliding mode loading, with predominantly shearing mode cracks requiring significantly larger fracture energy. The question of whether the interface will trap the crack or whether the crack will kink out into the more brittle side of the bimaterial interface was examined by a number of investigators. The kinked crack will grow if the cohesive fracture energy for a mode I crack in one of the constituents is smaller than the fracture energy for growing the combined opening-shearing mode crack along the interface [27]. Using an asymmetrically loaded edge-cracked geometry, Rosakis et al., [50] and Samudrala et al., [52] have grown interface cracks at high speeds and investigated a number of significant issues in the dynamic growth of these interface cracks. In particular, these investigations have demonstrated that mode II cracks trapped in weak planes may grow at speeds in the range from zero to the Rayleigh wave speed and then at speeds larger than the square root of two times the shear wave speed, but below the dilatational wave speed

[30, 31, 49, 53].

Obtaining the equation of motion for crack growth either in opening or shearing mode is the fundamental aim of continuum analysis of the dynamic crack growth problem. One expects to obtain a relationship between the crack driving force described in crack local terms through the dynamic stress intensity factor and the response characterized both by the amount of energy dissipated in the fracture and the speed with which the fracture grows. While the amount of energy dissipated in the fracture process in the ideal situation is simply the surface energy - presumably independent of the speed with which it is created - in real materials with microstructural features, one finds that the dissipation is dependent on the rate at which the fracture is propagated. Typically one would have to determine the energy dissipated from precise experiments or detailed models of the fracture process. Elastodynamic analyses of crack problems have therefore decoupled the equations of motion of the continuum from the fracture criterion and interpret the crack tip stress state through an analysis of the stress and deformation fields as well as a characterization of the energy flow into the crack tip region. Even without a detailed model of the fracture process, the elastodynamic calculations set certain limits for dynamic crack propagation. Broberg [8] has described these limits in great detail; we will review them in the Chapter 3.

In this work, we focus on shear crack growth in a homogeneous, isotropic material. Shear cracks can be nucleated and grown along the groove by introducing a groove in the specimen under a dominant shear loading parallel to the groove. Specially designed experimental system and some experimental results are described more detail in Chapter 3.

1.2 Frictional Sliding under Dynamic Loading

Friction between surfaces has been the subject of intense investigations from time immemorial! In recent years, while there has been a spurt of activities in understanding friction and adhesion at the atomic scale (driven primarily by the development/promise of MEMS and nanoscale devices), there has also been a renewed interest in understanding the dynamics of macroscopic constitutive description of friction, postulated in phenomenological terms, either through the simple model of Amontons-Coulomb or through the more sophisticated models developed by Dietrich [20] and Ruina [51] or from the experiments of Prakash [42] that account for rate of sliding and ageing effects. There has also been an emphasis on the propagation of crack like sliding and slip pulses at interfaces [2, 10, 36, 44, 59]. Examples of high speed contact sliding where such phenomenological models are quite important include rail-gun applications, where a projectile is accelerated along a track with significant normal pressure and sliding velocities in the range of 1 - 2,000 m/s at launch and earthquakes where slip in the form of pulses may travel at speeds faster than the shear wave speeds in the crust [4]. Oden and Martins [38] present a significant review of the literature on dynamic friction focusing primarily on metallic materials applicable to technological problems. There is also a vast literature on geophysical applications [28, 34].

In the last three decades there have been a string of analytical, numerical and limited experimental results on the dynamics of slip at high slip speeds that have provided the impetus for the current investigations. Two types of analyses have been considered in the literature: growth of a mode II crack with energy dissipation required to generate new surfaces across which frictional sliding occurs and slip pulse propagation along previously created frictionally held surfaces. Burridge [10] considered the self-similar extension of a mode II crack in a cohesionless interface between two identical materials with Coulomb friction - the mode II analog of the Broberg problem for mode I cracks - and found that the slip may propagate at the speed of the dilatational wave speed C_d without a singularity if the static friction is low. It should be noted that this analysis unifies the consideration of the problem of mode II crack propagation and frictional slip propagation. Andrews [3] modeled a mode II crack through a slip-weakening model for the crack tip cohesive zone and identified in numerical simulations that the growing shear crack nucleated a daughter crack ahead and accelerated to a speed of $\sqrt{2}C_s$(the speed regime between the shear wave speed and the dilatational wave speed is referred to as the intersonic regime, see Fig. 1.1).

Broberg [8] and Freund [23] analyzed the nature of the crack tip stress fields and energy flow into the crack tip region in mode II cracks and established that the crack tip possesses a square root singularity at the speed of $\sqrt{2}C_s$ and hence mode II cracks may grow at this speed. Broberg found that four different crack velocity regions can be identified in mode II (see Fig. 1.1)

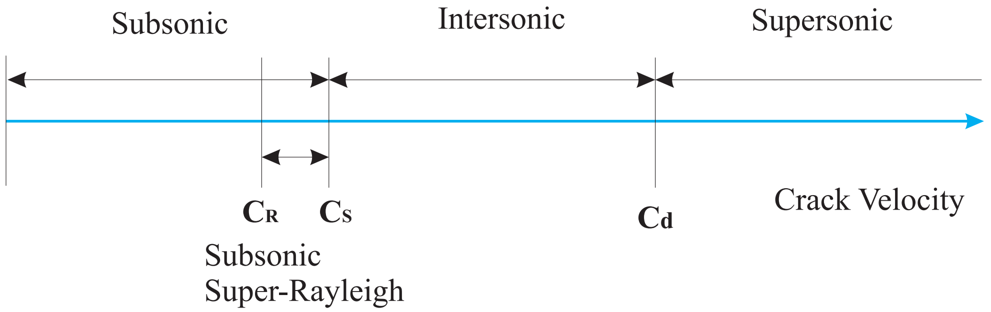

Figure 1.1: Crack speed regimes [8].

and that the crack cannot be propagated at the speed of range between the Rayleigh wave speed and the shear wave speed (the speed region is referred to as the subsonic super-Rayleigh region) due to the negative energy flow to the crack edge. Freund [23] studied shear crack propagation in the intersonic region and found that for mode II crack propagation the energy flux into the crack tip is zero for all speeds of this intersonic range except for the speed of $\sqrt{2}C_s$. More recent models based on a cohesive zone at the crack tip suggest that other intersonic speeds are attainable as well, either in an unstable or stable condition. However, few experimental results are available; Rosakis et al., [50] observed shear cracks in bonded bimaterial interfaces to propagate at $\sqrt{2}C_s$; this was the first direct measurement of intersonic crack growth under shear loading. Ravi-Chandar [45] demonstrated that even in homogeneous materials (without a weak interface), when trapped within a groove shear cracks may grow at speeds in the intersonic range by sequential nucleation of daughter cracks or echelon cracks; isochromatic fringe patterns from one such experiment in a Homalite-100 plate is shown in Fig. 1.2. From the abrupt

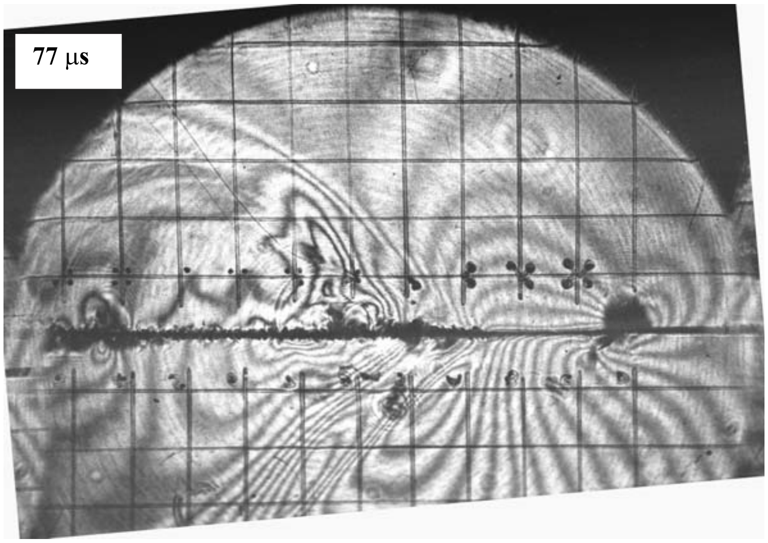

Figure 1.2: Isochromatics from an intersonic crack in Homalite-100 [45].

slope changes in the isochromatic fringes, the location of the shear Mach line can be identified; the ±45° inclination of the Mach line indicates that the crack is growing at a speed of $\sqrt{2}C_s$.

Weertman [59] showed that a self-healing slip pulse (initiating slip at its leading edge and terminating slip at its trailing edge) can be generated across a frictional interface between dissimilar materials. Weertman suggested that a self-healing slip pulse may propagate in an unstable manner even when the global stress state is subcritical for frictional slip. Adams [2] showed that frictional slip is indeed possible at intersonic speeds and determined the nature of the stress waves radiated from such a slip event under the assumption of Coulomb friction. Archuleta [4] suggested that frictional slip in earthquakes may propagate at speeds in excess of the shear wave speed and Heaton [28] proposed self-healing slip pulses to account for the short duration of slip at a point in comparison to the total duration of the earthquake. Xia et al [62, 63] have recently shown that frictional slip across interfaces with a quasi-static pre-stress can also grow into the intersonic regime. Numerous researchers [38, 44] have discussed the fact that the slip pulse propagation problem with Coulomb frictional model is ill-posed. Rice and co-workers have approached regularization through the use of a rate and state dependent constitutive model for friction. On the other hand, Martins [38] suggested that introducing a dependence on normal stress based on a length scale might regularize the problem. While this debate continues, the critical need is for some additional experimental insight into the nature of the frictional constitutive law at high slip speeds. It is evident that slip pulses may propagate at speeds in excess of the shear wave speed.

In this work, we focus on dynamic slip along a frictional interface between two materials. To do this, two different experimental schemes have been developed under extremely high rates of loading. In addition, the propagation characteristics of a slip pulse are presented and examined through dynamic photoelasticity in Chapter 4.

1.3 Outline of Dissertation

In this dissertation, we present the results from experiments aimed at investigating fracture and frictional sliding under shear loading conditions. The following is an outline of this dissertation.

In Chapter 2, we introduce a new apparatus developed for this study under extremely high rates of loading and demonstrate the application of dynamic photoelasticity to dynamic fracture and friction problems.

In Chapter 3, we examine shear cracks in homogeneous materials by introducing a groove in the specimen and trapping the crack to grow within it. Conditions for nucleation of cracks are determined from such experiments.

In Chapter 4, we examine the nature of dynamic slip events by direct observations of slip propagation in carefully controlled experiments. The propagation characteristics of this slip are then examined through dynamic photoelasticity. In addition, we introduce an experimental model to examine the dynamic slip under the release pressure ahead of the frictional interface and present some experimental results.

In Chapter 5, we introduce a new optical method by adopting classical methods of photoelasticity and Mach-Zehnder interferometry in a combined arrangement in order to determine both principal stresses and their orientations simultaneously. We will also show that this optical method eliminates the need for high-speed photographic system, but more importantly provides complete, time-resolved evolution of all stress components. In addition, some examples of application of the method are demonstrated.

Chapter 2

Experimental Procedure

A wide variety of techniques are used to produce stress waves in solids. Different experimental methods have been developed for the purpose of examining dynamic behavior of materials, since many materials exhibit different deformation behavior in different strain rate regimes. The range of strain rates (or loading rates) in different loading schemes is given in Fig. 2.1.

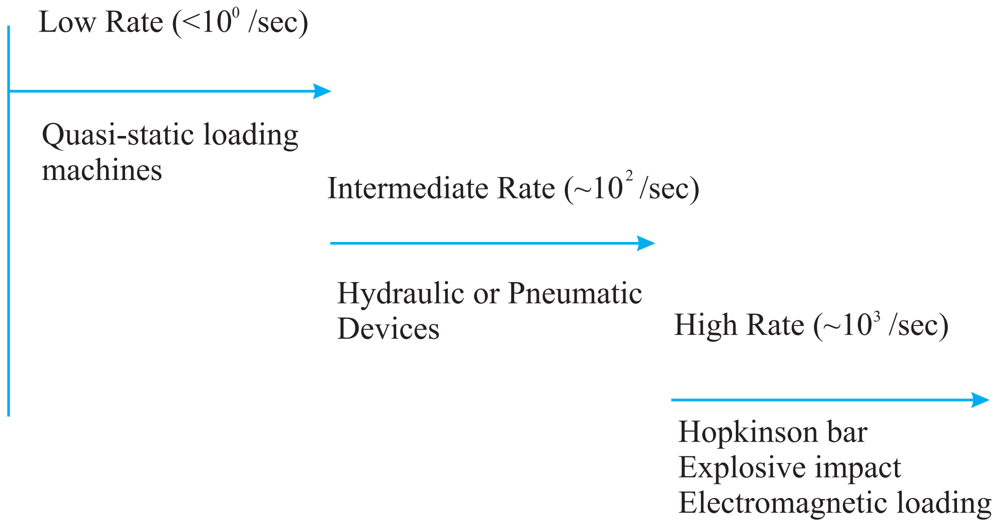

Figure 2.1: Range of strain rates obtained in different loading methods [65].

At low strain rates of the order of up to $10^0 s^{-1}$, the load is applied slowly and the uniaxial tension, compression curve with constant strain rate is used to describe the material behavior. Hydraulic or pneumatic devices are used to generate stress waves at intermediate strain rate regime from 10^{-1} to $10^2 s^{-1}$. The strain rates of the order of $10^3 s^{-1}$ or higher are generally considered as high strain rates. In this regime, strain rate and wave propagation effects are important in understanding the dynamic behavior of materials. Projectile impact, Hopkinson pressure bar, various types of explosives (such as Lead azide and pentaerythritol tetranitate (PETN)) and electromagnetic loading have been developed to generate high magnitude, short duration stress pulse loading. More detailed descriptions of the electromagnetic loading and projectile impact methods which are used in this chapter are presented below.

2.1 Electromagnetic Loading Device

Among dynamic loading methods used to generate stress waves, the electromagnetic loading scheme is quite simple and versatile. This loading scheme is based on electromagnetic interaction between two current carrying conductors (Ravi-Chandar and Knauss, [47]). A flat copper strip, 12.7 mm (0.5") in width by 0.53 mm (0.02") thickness is folded back with 3 loops which increase the input pressure and the space between the layers is filled with an insulating strip. When a current flows through the copper loop, each leg generates a magnetic field surrounding it. The magnetic field oriented normal to the current vector interacts with the current vector of the other leg to produce an electromagnetic repulsion that forces the conductors apart. This electromagnetic force is impressed upon the surface of the plate in order to generate a uniform pressure. The magnitude of the pressure loading may be estimated easily from electromagnetic theory as follows:

$$P(t) = \frac{1}{2}\mu_0 \left(\frac{i(t)}{b}\right)^2 \tag{2.1}$$

where $P(t)$ is the pressure of repulsion, b is the width of conductors and $\mu_0 = 4\pi \times 10^{-7}$(weber / amp-m) is the permeability constant. The current in the copper strip, $i(t)$, is generated by a discharge from a capacitor bank. The time history of the current which dictates the magnitude and duration of the pressure applied on the surface of the specimen may be controlled by suitable choice of capacitors and inductors that form the pulse, with a rise to the peak amplitude in about $25\mu s$, and a total duration of about $150\mu s$. In case of the 3 loop copper strip used in the experiments, the surface pressure is larger than a single loop copper strip. In our experiment, a pressure of 35.6 MPa is generated at approximately 5000 volt in the capacitor.

2.1.1 Charge-Discharge Circuits

To supply the current to the copper strip for generating the electromagnetic force, an electric circuit consisting of capacitor, inductor and resistor shown in Fig. 2.2 is used. As shown in the figure, the charge-discharge circuit consists of 11 capacitors with capacitance (C) of $25\mu F$, 11 inductors, an ignitron switch and a capacitor charging power supply. The circuit can store energy up to 60 kJ at 20 kV and the discharge is controlled through the

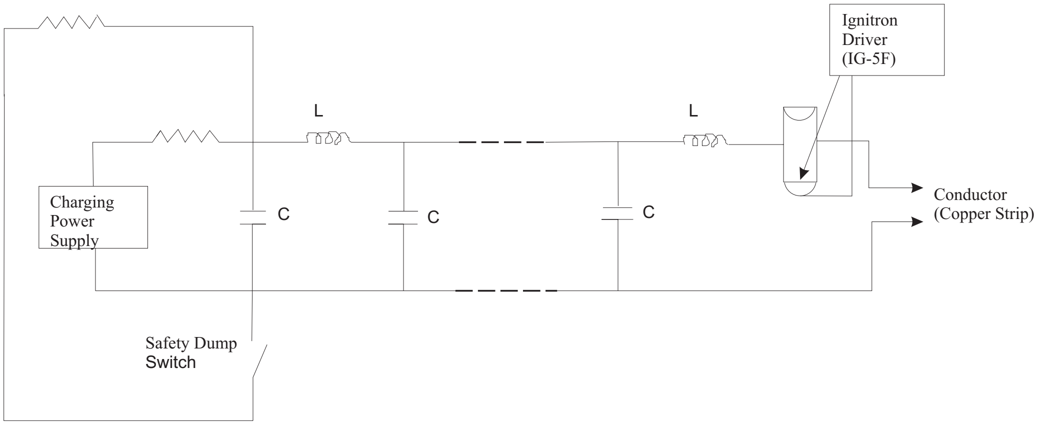

Figure 2.2: The configuration of the charging and discharging circuit: 11 Capacitors (C=25μF) and 11 Inductors.

ignitron switch which is controlled by the firing module (IG5F). This model (IG-5 Ignitron driver, Richardson Electronics Co.) is designed to meet the specifications for triggering all ignitrons and is triggered by the 5V TTL signal sent through a fiber optic cable. Consequently, the IG-5 Ignitron switch is triggered through the signal from the main system controller and this triggers the ignitron switch leading to discharge of the capacitors through the copper strip.

The capacitor charging power supply is connected to the capacitor bank by a resistor to charge the system. Another discharge circuit is connected to the capacitor bank for safety; the purpose of this circuit is to prevent the capacitors to be charged unintentionally after the test.

2.1.2 Calibration of the Loading Device

The Rogovski coil measures the current flowing in the copper strip. The advantage of this method is that it does not need any direct connection between the measuring circuit and the current path. The Rogovski coil measures the current rate indirectly using a toroidal winding. The voltage induced in the coil is proportional to the rate of change of current. The resulting voltage needs to be calibrated in terms of the current rate in the copper strips. This is done by connecting to the copper strips only one of the capacitors and one inductor. The detailed procedure for calibration is presented in Appendix A. The resulting output is a decaying sine wave as shown in Fig. A.2, the amplitude of which could be calculated as follows:

$$\dot{I}_{T/2} = -CV_0 \left(\frac{2\pi}{T}\right)^2 \left(\frac{A_3}{A_1}\right)^{\frac{1}{2}} \tag{2.2}$$

where $\dot{I}_{T/2}$ is the current rate at 1/2 period in amps, V_0 is the charge voltage in capacitor in volts, C is the capacitance in farads, T is the period in seconds and A_3/A_1 is the ratio of successive peaks of same sign. From the calibration tests for specified voltages, A_3/A_1 and T can be determined. Using the given values V_0 and C (in our experiment system, $C = 25\mu F$), we can calculate the current rate from Eq. (2.2). This value also yields a known voltage (V_R) from the Rogovski coil. Hence 1 volt of Rogovski output can be related to the current rate of the copper strip in amps/s. The period was $45\mu s$ for all cases with a combination of one capacitor and one inductor. From this calibration, the calculated calibration factor between the current rate in the copper strips and the integrated Rogovski coil output is that 1 Voltage in the integrated Rogovski coil output $\cong$ 38 MA/s in the copper strips.

2.1.3 Electromagnetic Loading

When current flows through a conductor, it produces a magnetic field. The magnetic field oriented normal to the current vector interacts with the current vector of the other leg to produce an electromagnetic repulsion that forces the conductors apart. The magnitude of the applied pressure which is proportional to the current in the copper strip can be calculated by using Eq. (2.1). The current shape from this circuit can be controlled by changing the total combination of the capacitors and inductors. The time history of the calculated stress pulse for a charging voltage of 5000 V for 11 capacitors and 11 inductors is shown in Fig. 2.3. Increasing the number of capacitors and inductors, results in the shape of the stress pulse becoming closer to an ideal square shape. The calculated peak pressure from the Eq. (2.1) as a function of the charge voltage is shown in Fig. 2.4

2.2 Projectile Impact

Projectile impact is one of the methods of generating dynamic loading, especially in high strain rate applications such as the Hopkinson pressure bar. The duration of the loading pulse depends on the length of the projectile while the magnitude of the loading pulse depends on the velocity of the projectile and material properties of the specimen. Based on one-dimensional wave theory,

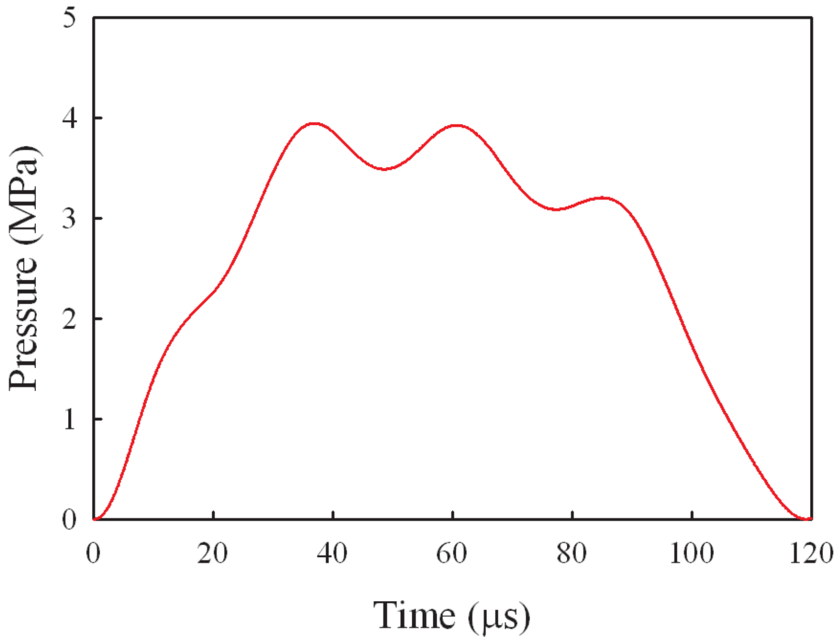

Figure 2.3: The time history of the stress pulse from a discharging circuit: 5000V, 11 capacitors.

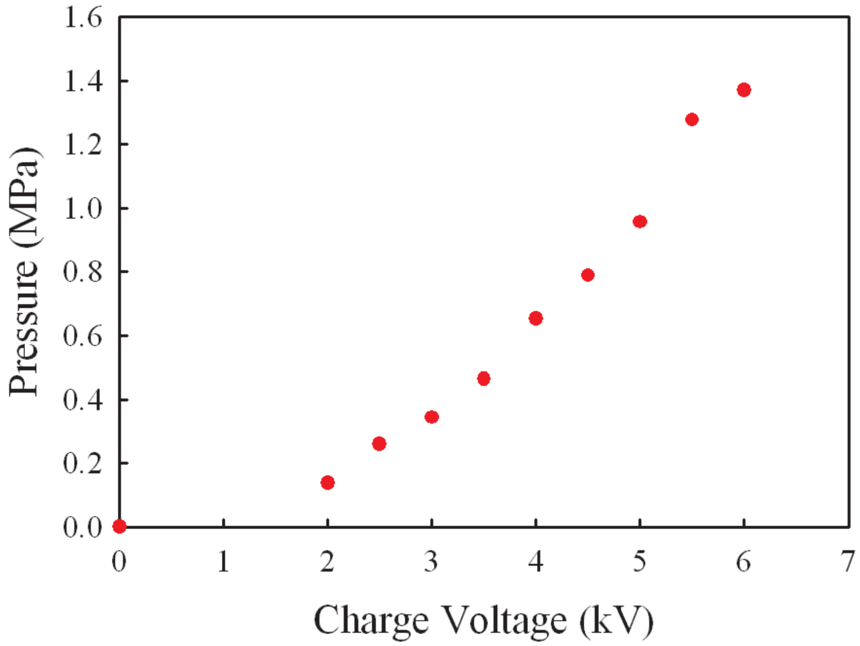

Figure 2.4: The generated pressure from the electromagnetic loading device for a single loop arrangement.

the duration and magnitude of the loading pulse are $\tau = 2L/C_0$ and $\sigma = \rho C_0 v_0$ respectively for a bar impacting another bar of the same impedance where L is the length of the projectile, C_0 is the bar wave speed in the projectile, ρ is the density and v_0 is the velocity of the projectile. With this method, a wide range of loading rates can be obtained by controlling the velocity of the projectile. The generated compressive loading pulse is quite repeatable.

In our experiments, a 50 mm diameter 100 mm long polycarbonate projectile was launched by an air-gun and accelerated through the barrel of a gun at speeds in the range of a 20 to 80 m/s. As shown in Fig. 3.3 (See Chapter 3), the projectile is made to impact the specimen at the desired location in order to generate dynamic loading. With this configuration, a compressive stress pulse can be generated to promote shear fracture in a homogeneous, isotropic specimen as described in more detail in Chapter 3.

2.3 Diagnostics

Dynamic photoelasticity has played a large role in the development of dynamic fracture mechanics. An early application of photoelasticity to dynamic fracture problems was demonstrated by Wells and Post [60], and this was followed by many others [18, 58]. While many of the studies of dynamic fracture problems included the use of photoelasticity, other full-field optical methods have also been developed and used. For example, Epstein et al. [21] and Pfaff et al. [40] used moir*é* and Twyman-Green interferometry, respectively, to examine the evolution of dynamic displacement fields. These methods place significant demands on the optical system for faithful recording of interference images. Chao et al. [12] applied the digital image correlation method to examine the dominance of the K-field in dynamic fracture; while this method is simpler than optical interferometric methods, it has not been used extensively. Tippur et al. [56] developed a lateral shearing interferometry technique to determine the out-of-plane displacement gradients and applied the technique to numerous dynamic crack problems; variants of this method are as easy to implement as photoelasticity, but again, very few investigators have used shearing interferometry in dynamic fracture studies. In short, full-field optical techniques have a major role in the development of dynamic fracture mechanics. In this section, dynamic photoelasticity is reviewed as the main diagnostic tool used to measure the stress field within the specimen.

2.3.1 Dynamic Photoelasticity

The method of the photoelasticity is based on the physical behavior of transparent materials. In some materials the index of refraction is affected by the application of external load. This behavior, known as temporary double refraction (birefringence), was first observed by Sir David Brewster [6]. Eqs. (2.3) $\sim$ (2.5) are the fundamental relationships between stress and optical effects and are known as the stress-optic law which describe the changes in index of refraction due to applied stress in a material exhibiting temporary double refraction.

$$n_1 - n_0 = c_1\sigma_1 + c_2(\sigma_2 + \sigma_3) \tag{2.3}$$

$$n_2 - n_0 = c_1\sigma_2 + c_2(\sigma_3 + \sigma_1) \tag{2.4}$$

$$n_3 - n_0 = c_1\sigma_3 + c_2(\sigma_1 + \sigma_2) \tag{2.5}$$

where σ_1,σ_2 and σ_3 are the principal stresses at a point, n_0 is the isotropic, unstressed index of refraction, n_1,n_2 and n_3 are the principal indices of refraction which coincide with the principal stress directions and c_1 and c_2 are the constants known as the direct and transverse stress-optic coefficients. For plane stress conditions, σ_3 can be set equal to zero. Furthermore, for light rays propagating in the x_3 direction, only the refractive indices n_1 and n_2 are of interest. Hence, Eqs. (2.3)∼(2.5) reduce to:

$$n_1 - n_0 = c_1\sigma_1 + c_2\sigma_2 \tag{2.6}$$

$$n_2 - n_0 = c_1\sigma_2 + c_2\sigma_1 \tag{2.7}$$

The relative angular phase shift Δ between the two components when the light beam passes through the stressed specimen can be written as:

$$\Delta = \frac{2\pi h}{\lambda}(n_2 - n_1) = \frac{2\pi hc}{\lambda}(\sigma_1 - \sigma_2) \tag{2.8}$$

where h is the thickness of a doubly refracting plate, λ is the wavelength of the light, and $c = c_1 - c_2$.

The photoelastic arrangement with four optical elements and a light source called the circular polariscope is illustrated in Fig. 2.5. The light beam polarized along the axis of polarization is then resolved into two components E_f and E_s vibrating parallel to the fast and slow axes through the first quarter wave plate. Since the axes of the quarter wave plate are oriented at $\pi/4$ with

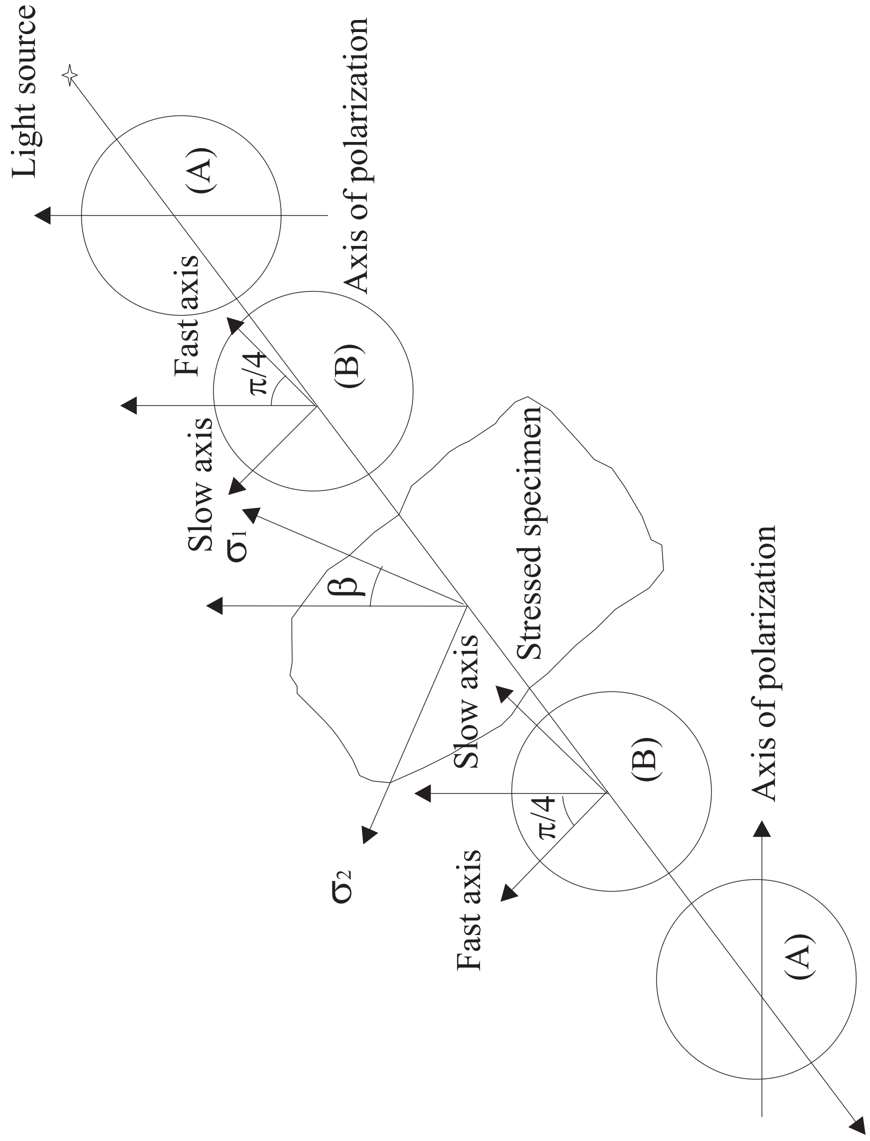

Figure 2.5: A photoelastic arrangement in a circular polariscope in a dark field configuration (A) Polarizer (B) Quarter wave plate [19].

respect to the axis of the polarizer and two components have a relative angular phase shift $\Delta = \pi/2$. Since the stressed specimen also acts as a wave plate, the additional relative retardation Δ (see Eq. (2.8)) is added as the light passes through the specimen. Similar to the first quarter wave plate, the light beam from the specimen is resolved into two components associated with the fast and slow axes of the second quarter wave plate and accumulate and additional phase shift of $\Delta = \pi/2$. Finally, the only vertical components of the light emerging from the 2nd quarter wave plate can be passed through the last polarizer. This output wave is given by (see Dally and Riley [19])

$$E_{out} = k \sin \frac{\Delta}{2} \sin(\omega t + 2\alpha - \frac{\Delta}{2}) \tag{2.9}$$

From the Eq. (2.9), the intensity of this light beam is given by:

$$I = k^2 \sin^2 \frac{\Delta}{2} \tag{2.10}$$

From Eq. (2.10) it is evident that the intensity reaches a minimum when $\Delta/2 = n\pi, n = 0, 1, 2, 3, ...$ Combining Eqs. (2.8) and (2.10) we write:

$$\sigma_1 - \sigma_2 = \frac{N f_\sigma}{h} \tag{2.11}$$

where $N = \Delta/2\pi$ is the isochromatic fringe order and $f_\sigma = \lambda/c$ is the material fringe value. Loci of constant intensity points define lines of constant $(\sigma_1 - \sigma_2)$ and are called isochromatics. From the Eqs. (2.8) and (2.10), it is seen that the intensity of the beam is not a function of the angle β. The mechanical and optical properties of two photoelastic materials are shown in Table 2.1. In our experiments, the isochromatic fringe patterns are captured using a high-speed

Table 2.1: Mechanical and optical properties of photoelastic materials [46].

Properties	Material	
	Polycarbonate	Homalite-100
Young's Modulus, $E (GPa)$	2.6	4.5
Poisson's Ratio, ν	0.4	0.34
Density, $\rho (kg/m^3)$	1230	1230
Dilatational Wave Speed, $C_d (m/s)$	1826	2057
Shear Wave Speed, $C_s (m/s)$	899	1176
Index of refraction, n	1.6	1.56
Material stress fringe value, $f_\sigma (kN/m)$	6.6	22.2

camera at short time intervals to provide a time history of the evolution of the shear stresses in the specimen.

2.3.2 High Speed Photography

The high speed camera and photoelastic arrangement used in this work are shown in Fig. 2.6. The high speed camera consists of an Argon ion pulsed laser as the light source and appropriate optical system including lenses and camera. The light beam passes through the specimen and is collected into the camera. In our system, 120 laser pulses with $11 \mu s$ period form 120 images on the circular 35 mm film located in the track. Our tests are conducted at 90,000 frames per second using a field of view of 75 mm (3") in diameter.

2.4 Timing Circuits

In order to obtain diagnostic images with the proper time sequence, it is necessary to adjust the triggering time for each system such as ignitron,

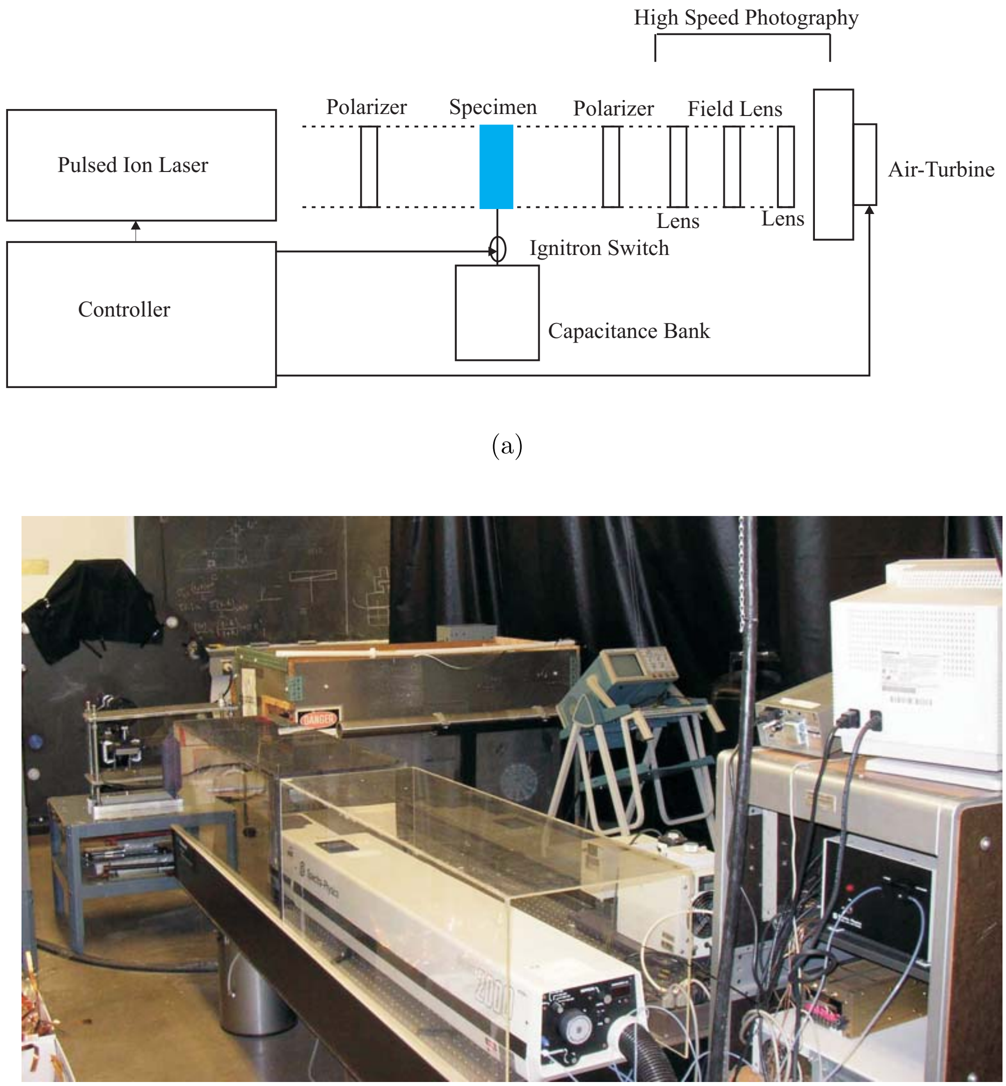

(a)

(b)

Figure 2.6: The entire experimental setup of dynamic photoelasticity including high speed photography.

shutter, and laser. The appropriate firing time for each system is controlled by programmed software with appropriate delay times. The timing diagram is shown in Fig. 2.7. The shutter for the high speed camera has internal delay time about 55 ms due to its mechanical components but remains open for 13 ms at 1/125 s shutter speed. This is not short compared with the total running time of experiment which is less than 1 ms. As shown in Fig. 2.7, the ignitron and laser must be controlled by suitable delays in order to trigger them after opening the shutter. Therefore, the shutter is triggered first with a delay D_1. It opens at $D_1 + 55$ ms and remains open until $D_1 + 55 + 13$ ms. Images are then acquired beginning at $D_3 > D_1 + 55$ ms so that the shutter is fully open. The ignitron is then fired at time $D_2 = D_3 + 0.19$ ms so that loading is applied at 0.19 ms after the beginning of images.

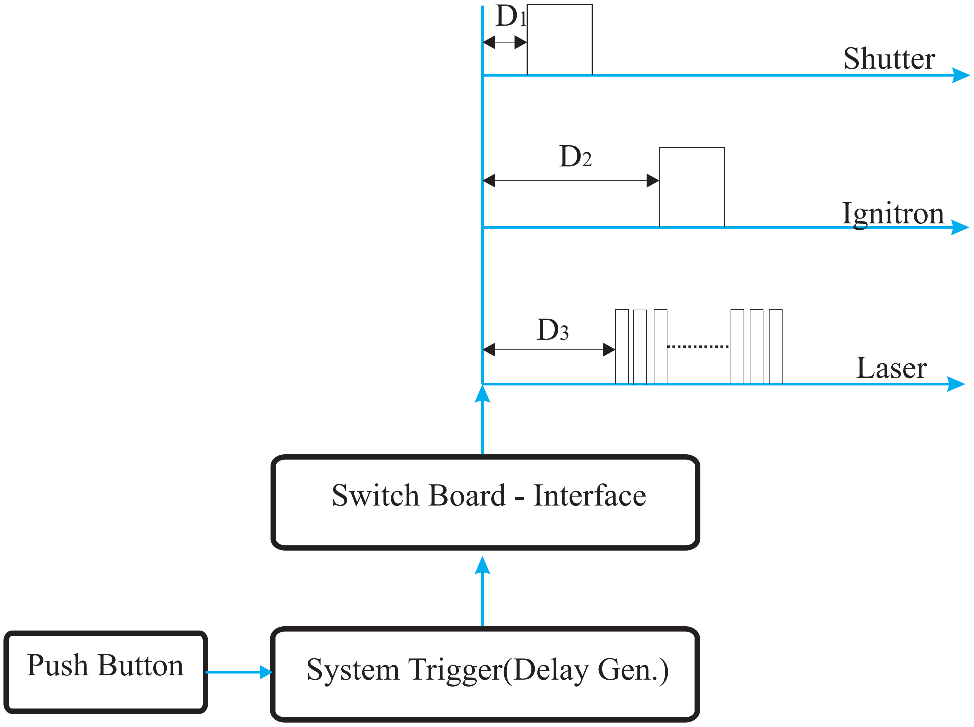

Figure 2.7: Delay time diagram for triggering systems.

Chapter 3

Dynamic Shear Induced Crack Growth

Dynamic fracture problems in solids have been studied intensively for nearly five decades. While most researchers have focused on crack problems under opening mode or mode I type of loading, recently there has been an emphasis on shear induced cracks in interfacial fracture, earthquake mechanics and high speed sliding. For example, Rosakis and co-workers [50] observed shear-dominated crack propagation along a weak plane that exceeded the speed of shear waves. The range of speeds between the shear and dilatational wave speeds is called the intersonic regime. In this chapter, we examine shear cracks in homogeneous materials by introducing a groove in the specimen and trapping the crack to grow within it. This does not affect the fracture mechanisms inherent to the material, but influences the energy flux and loading symmetry. We demonstrate that such shear induced cracks can grow at speeds in the intersonic regime. Furthermore, it is shown that the main mechanism of the shear crack growth is the sequential nucleation, growth and coalescence of echelon cracks. The spacing and angle relative to the groove plane of the echelon cracks are measured directly from the experimental specimen. Numerical simulation shows that the echelon cracks are well aligned perpendicular to the maximum principal (tensile) stress generated in this specimen. The spacing is interpreted as an intrinsic characteristic of the failure process. These experiments also enable the determination of the dynamic failure stress at which microcracks are nucleated.

3.1 Asymptotic Stress Field for Crack Growth under Mode II Loading

The asymptotic stress fields for cracks moving at a speed v have been obtained for all possible modes of loading on the crack. The general procedure for derivation of these fields may be found in Freund and Clifton [25]. The structure of the field depends on the crack speed and the mode of deformation. We denote C_d and C_s as the dilatational and distortional wave speeds respectively. If $v < C_s$, the crack is said to be subsonic and the Cartesian components of the stress field for mode II symmetry can be written as follows [24]:

$$\sigma_{\alpha\beta}(r,\theta) = \frac{K_{II}}{\sqrt{2\pi r}} f^{II}_{\alpha\beta}(\theta; v) \quad as \quad r \rightarrow 0 \tag{3.1}$$

$$\begin{aligned} f^{II}_{11}(\theta; v) &= -\frac{2\alpha_s}{R(v)}\{(1+2\alpha_d^2-\alpha_s^2)\frac{\sin\frac{\theta_d}{2}}{\gamma_d^{\frac{1}{2}}} - (1+\alpha_s^2)\frac{\sin\frac{\theta_s}{2}}{\gamma_s^{\frac{1}{2}}}\} \\ f^{II}_{22}(\theta; v) &= \frac{2\alpha_s(1+\alpha_s^2)}{R(v)}\{\frac{\sin\frac{\theta_d}{2}}{\gamma_d^{\frac{1}{2}}} - \frac{\sin\frac{\theta_s}{2}}{\gamma_s^{\frac{1}{2}}}\} \\ f^{II}_{12}(\theta; v) &= \frac{1}{R(v)}\{4\alpha_d^2\alpha_s^2\frac{\cos\frac{\theta_d}{2}}{\gamma_d^{\frac{1}{2}}} - (1+\alpha_s^2)\frac{\cos\frac{\theta_s}{2}}{\gamma_s^{\frac{1}{2}}}\} \end{aligned} \tag{3.2}$$

$$\gamma_d = \sqrt{1-(v\sin\theta/C_d)^2} \quad and \quad \gamma_s = \sqrt{1-(v\sin\theta/C_s)^2} \tag{3.3}$$

$$\tan\theta_d = \alpha_d \tan\theta, \tan\theta_s = \alpha_s \tan\theta \tag{3.4}$$

$$R(v) = 4\alpha_d^2\alpha_s^2 - (1+\alpha_s^2)^2 \tag{3.5}$$

$$\alpha_d = \sqrt{1-\frac{v^2}{C_d^2}}, \alpha_s = \sqrt{1-\frac{v^2}{C_s^2}} \tag{3.6}$$

Polar coordinates (r, θ) centered at the moving crack tip are used in the above equations. From Eq. (3.1), it is clear that the stress field is singular as the crack tip is approached with the familiar square root singularity observed in the corresponding quasi-static problem. The strength of the singularity is the dynamic mode II stress intensity factor, K_{II}, defined as follows:

$$K_{II}(t) = \lim_{r\to 0}(2\pi r)^{1/2}\sigma_{12}(r, 0, t) \tag{3.7}$$

The dynamic energy release rate per unit area can be calculated by considering the flux of energy into the crack tip region and is given as [24]:

$$G = \frac{1-\nu^2}{E}A_{II}(v)K_{II}^2, \quad A_{II}(v) = \frac{v^2\alpha_s}{(1-\nu)C_s^2 R(v)} \tag{3.8}$$

where E and ν are the modulus of elasticity and Poisson's ratio respectively. From a fundamental physical point of view, for a crack growing at a speed v, this energy release rate must be equal to the dissipation in the fracture process zone. Considering the singularity in the function $A(v)$ at the Rayleigh surface wave speed, a subsonic mode II crack is limited to propagate below speed. Interface cracks in this regime were examined by Lambros and Rosakis, [31]. Ravi-Chandar et al. [48] demonstrated that in polymethylmethacrylate (PMMA), ductile cracks that grew as pure mode II cracks trapped in a groove were indeed limited to grow below the Rayleigh wave speed.

If $C_s < v < C_d$, the crack is in an intersonic regime; the analysis of shear cracks that run in this speed range has been considered by some researchers [8, 11, 23, 54]. Expressions for the variation of the crack tip stress field in polar coordinates (r, θ) are given in [9]:

$$\begin{aligned} \{\sigma_{rr}, \sigma_{\theta\theta}\} = & -\frac{A}{r^g}\frac{(1-k^2)(1+\hat{\alpha_s}^2)}{2\alpha_d}\frac{\sin g\theta_d}{T_P} \\ \mp\frac{A}{r^g}\{ & \frac{\cos 2\theta}{2\alpha_d}[(1+\alpha_d^2)\frac{\sin g\theta_d}{T_P} + (\hat{\alpha_s}^2 - 1)\frac{\sin \pi g}{T_S}H(|\theta| - \theta_f)] \\ & - \sin 2\theta[\frac{\cos g\theta_d}{T_P} + \frac{(\hat{\alpha_s} - 1)^2}{4\alpha_d\alpha_s}\frac{\sin \pi g}{T_S}H(|\theta| - \theta_f)]\} \end{aligned} \tag{3.9}$$

$$\begin{aligned} \sigma_{r\theta} = \frac{A}{r^g}\{ & \frac{\sin 2\theta}{2\alpha_d}[(1+\alpha_d^2)\frac{\sin g\theta_d}{T_P} + (\hat{\alpha_s}^2 - 1)\frac{\sin \pi g}{T_S}H(|\theta| - \theta_f)] \\ & + \cos 2\theta[\frac{\cos g\theta_d}{T_P} + \frac{(\hat{\alpha_s} - 1)^2}{4\alpha_d\alpha_s}\frac{\sin \pi g}{T_S}H(|\theta| - \theta_f)]\} \end{aligned} \tag{3.10}$$

$$k = \frac{C_s}{C_d}, \quad \hat{\alpha_s} = \sqrt{\frac{v^2}{C_s^2} - 1}, \quad \sin\theta_f = \frac{C_s}{v} \tag{3.11}$$

$$T_P = [\cos^2\theta + \alpha_d^2 \sin^2\theta]^{g/2}, \quad T_S = [|\cos\theta| - \hat{\alpha_s}|\sin\theta|]^g \tag{3.12}$$

$$g(v) = \frac{1}{\pi}\tan^{-1}\frac{4\alpha_d\hat{\alpha_s}}{(\hat{\alpha_s}^2 - 1)^2}, \quad 0 < g \leq \frac{1}{2} \tag{3.13}$$

$H(|\theta| - \theta_f)$ represents the unit step function. From Eqs. (3.9) and (3.10), it is seen that the stress field is singular as the crack tip is approached, with the nature singularity given in Eq. (3.13) indicating a velocity dependence. Clearly the singularity is weaker than the subsonic square root singularity with one exception to be discussed below. The strength of the singularity, A, is defined as follows:

$$A = \lim_{r \to 0}(2\pi r)^g \sigma_{12}(r, 0, t) \tag{3.14}$$

and plays a role similar to the stress intensity factor in the subsonic case. Two key distinguishing features of the intersonic stress field shown in the equations above are important to recognize; first, the presence of terms indicated by the unit step function, suggests a possible discontinuous change across the radial lines $|\theta| = \theta_f$. This is a manifestation of the fact that the crack moves faster than the shear waves emanating from the crack tip and results in the Mach waves as indicated in Fig. 3.1. Second, an estimate of the order of

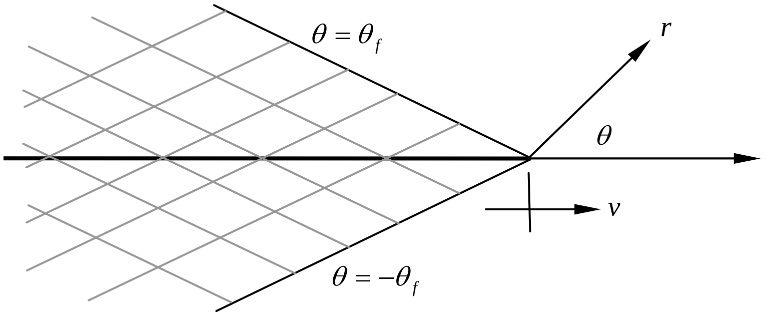

Figure 3.1: The crack is moving with a speed $v > C_s$. Contributions from the shear waves to the stress field arise only for $|\theta| > \theta_f$.

energy release rate for intersonic crack growth can be obtained simply as the product of the stress and displacement components; thus, $\sigma_{12} \sim Ar^{-g(v)}$, $u_1 \sim Ar^{-g(v)+1}$ implies that the energy release rate $G \sim \sigma_{12}u_1 \sim A^2r^{-2g(v)+1}$; the energy release rate tends to zero as $r \to 0$ for all cases except when $g(v) = 1/2$. This exception occurs when $v = \sqrt{2}C_s$; at this speed, a square root singularity is recovered and a finite energy release rate is possible. Hence, an intersonic crack can propagate at this speed. It should be noted that the terms involving the unit step functions disappear completely at this speed suggesting that the shear wave does not contribute to the crack tip stress field. In the experiments discussed in this chapter, we will implement loading conditions appropriate to generate intersonic cracks and interrogate them with dynamic photoelasticity. Therefore, we use the asymptotic stress fields indicated in Eqs. (3.1), (3.9) and (3.10) to simulate typical patterns of isochromatics for comparison with the experiments. Such patterns are shown in Fig. 3.2 for the subsonic and intersonic cases. The isochromatic fringe pattern in Fig. 3.2 (a) corresponds to a subsonic crack under pure mode II loading; there are many experimental observations of such fringe patterns. The fringes in Fig. 3.2 (b) correspond to an intersonic crack propagating at $v/C_s = \sqrt{2}$; the absence of discontinuities at this velocity are evident from the figure. Freund [23] showed that if a cohesive zone is introduced at the crack tip with a prescribed traction-sliding velocity relationship, speeds in the interval $\sqrt{2}C_s \leq v \leq C_d$ also lead to finite energy release rate and hence intersonic mode II cracks may propagate with speeds in this range. With the understanding that the process zone (or the sliding zone) is small, the analysis indicated here should hold for both cracks and frictionally held interfaces.

3.2 Experimental Set-up for Dynamic Shear Crack Growth

Our interest is in observing shear crack growth in a homogeneous material, without heterogeneity or anisotropy in either the fracture or the constitutive properties of the material. The key idea needed to accomplish this

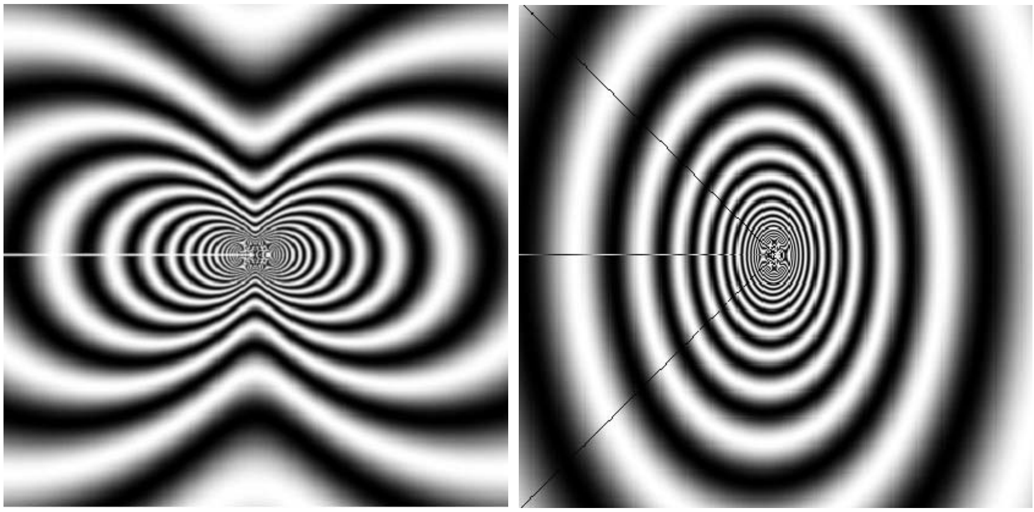

(a) (b)

Figure 3.2: Simulated isochromatic fringe patterns corresponding to a dark field circular polariscope arrangement. (a) subsonic crack growth with $K_{II} = 1MPam^{1/2}$ and $v/C_s = 0.2$;(b) intersonic crack growth with $A = 0.3MPam^{1/2}$ and $v/C_s = \sqrt{2}$. Fringe constant $f_\sigma = 7kN/m$ corresponding to polycarbonate. The field of view shown in these figures is 40 mm to a side.

- confining pressure - is already present in the quasi-static experiments of von Karman [57], Wong [61] and Broberg [7]. However, if one generates such confinement, it becomes difficult to observe the crack tip motion in real-time; furthermore, the confinement introduces additional frictional contact along the crack surfaces, further complicating the energy dissipation during fracture. We describe an experiment where a groove is used to trap a mode II crack along a specific plane; this approach has been used by Cotterell [16] to suppress crack branching under mode I loading and to grow faster mode I cracks; Broberg [8] also hinted at the possibility of using this configuration for shear mode cracks. We resort to the asymmetrically loaded geometry, with a groove as illustrated in Fig. 3.3; in initial experiments, a precrack was used, but in later experiments, we dispensed with the crack altogether and investigated a grooved specimen. Spontaneous crack nucleation was then observed.

It is important to emphasize the role of the groove - what it is, what it does and more importantly what it does not do. The detailed geometry of the groove is shown inset in Fig. 3.3; it was introduced simply by cutting with a saw blade in a mill. It increases the in-plane shear stress imposed on the material along the groove plane; there might be some high frequency influence arising from the geometric changes, but we expect that in the long term (on the order of 50 to 100 μs) these might not play a big role. We will show that this is indeed the case through an examination of the stress field developed in the experiment. The groove also produces a stress concentration at the groove tips that might appear crack-like; crack initiation and growth in the thickness

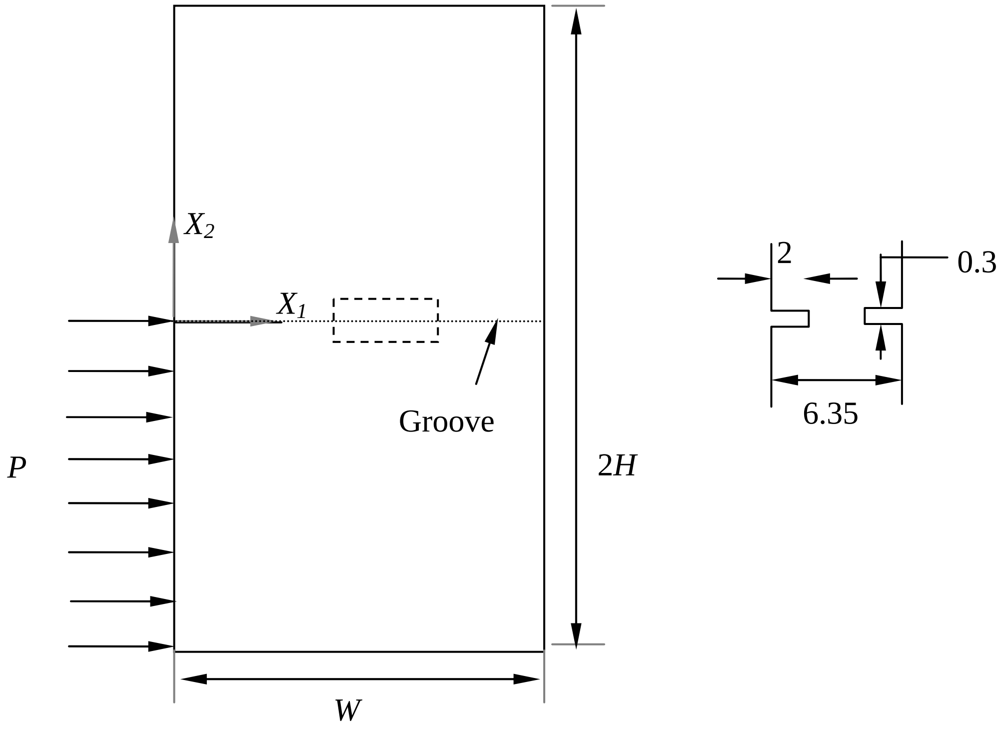

Figure 3.3: Asymmetrically impacted specimen geometry for dynamic mode II experiments. Details of the groove with dimensions in mm are shown on the right.

direction is a distinct possibility. The main role of the grooves, at least the role we hope that they would play, is to change the ratio of energies for mode II and mode I fracture. But the most important feature of the experimental investigation is that *the lowering of the total energy required for mode II crack growth is accomplished without altering the toughness or the strength of the material.* The mechanisms of deformation and fracture in opening and shearing modes are left unaltered and will develop as dictated by the evolution of the stress field, unlike in a weak interface, where they are clearly altered.

The experimental arrangement is shown schematically in Fig. 3.3. The grooved specimen is impacted with a polycarbonate projectile accelerated to speeds in the range of 20 to 80 m/s by an air-gun. A high-speed camera capable of 100,000 frames per second with exposure times of around 15 ns was used to capture the wave propagation, crack initiation and growth. Homalite-100, a thermosetting polyester (supplied by SGL Homalite) was used as the specimen material. Relevant material properties are listed in Table 2.1. Homalite is a strongly birefringent material and hence the specimen was observed in a circular polariscope providing *isochromatic fringes* or contours of constant shear stress [46]. Two sets of experiments were performed: in the first set, two Homalite-100 specimens, one without a groove and the other with a groove were impacted at the same speed and the evolution of the isochromatic fringe patterns was observed. The main objective of this experiment is to demonstrate the exact role of the grooves in the transmission of the deformation from one side to the other. In the second set, Homalite specimens with grooves, but without cracks, were impacted at different speeds. Even in the absence of an initial crack, the stress enhancement induced in the groove plane is sufficient to trigger crack nucleation and growth. We now discuss each one of these sets of experimental observations in detail.

In our attempt to promote shear fracture, we have introduced a groove in the specimen; the influence of the groove on the development of the stress field can be determined by performing a detailed three dimensional finite element analysis where the groove will by necessity be represented by an idealized description of the geometry. On the other hand, the influence can be determined exactly very simply by performing two experiments at nominally the same conditions on two specimens, one with a groove and one without and comparing the evolution of the isochromatic fringe patterns; this is a powerful illustration of the simplicity and elegance of photomechanics! In Fig. 3.4, three selected frames from two tests are shown at very nearly corresponding times. Since the synchronization of the picture sequence with the impact event could be delayed by a few microseconds, exact time matches are difficult to obtain; however, the differences are within $5\mu s$, and the dilatational wave travels only about 10 mm in this time, so meaningful comparisons of the stress field evolution may be obtained from the sequence of pictures shown. The top row in Fig. 3.4 corresponds to a Homalite specimen without a groove, impacted at about 33 m/s. The bottom row in Fig. 3.4 also corresponds to a Homalite specimen impacted at a speed of about 34 m/s, but this specimen contains a groove. Comparing the two sequences of photographs, it is clear that the

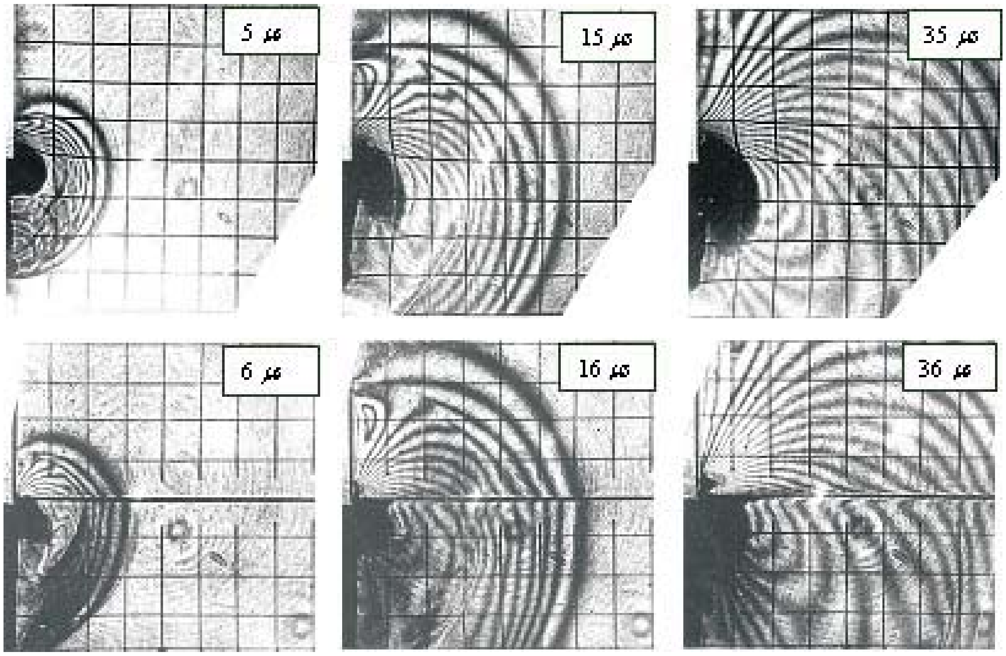

Figure 3.4: Evolution of the dynamic stress field under asymmetric impact in a Homalite-100 specimen; top row shows specimen without a groove; the bottom row shows the influence of the groove. Square grid is 6.35 mm (0.25 in) to a side.

development of the isochromatic fringe patterns is quite similar in the two specimens, especially in the top portion of the specimen whose stress evolution is controlled by the energy transferred across the groove. This observation is taken as an assurance that the effect of the groove on the development of the overall stress field was not significant far away from the groove; note, however, that there is a concentration of shear along the groove line as indicated by the steep gradients in the density of isochromatics in the bottom row of Fig. 3.4 which focuses the failure to develop in this plane. Thus, the presence of the groove does not disturb the evolution of shear stresses globally, but produces as expected an enhanced shear in the plane of the groove; the groove provides the appropriate stress field for the development of a shear fracture as described next.

3.3 Shear Induced Crack Nucleation and Growth

In the experiments performed without a groove, the specimen simply takes the kinetic energy from the projectile and flies off towards a catcher tank without fracture or fragmentation. On the other hand, the stress concentration in the groove causes crack nucleation and growth from different locations on the specimen depending on the impact speed. With increasing impact speed, crack nucleation was observed in the interior of the specimen, at the far end from impact, and at the impact end. Here, we examine nucleation of cracks in the interior of the specimen.

The propagation of stress waves from uniform pressure loading on a

Homalite-100 specimen is shown in Fig. 3.5. Four frames beginning at 55 μs after impact at 11 μs time increments are shown. The width of the specimen is 101.6 mm (4 in) and the dilatational wave travels across the specimen, reflects at the traction-free distal boundary and returns towards the impact end; when this wave interacts with the shear wave generated by mode conversion at the corner of the impact point, a large increase in shear stress arises and cracks are nucleated at this point (this corresponds to about 75 μs and corresponds to the 3^{rd} frame shown); this crack proceeds from the nucleation point marked on the figure and follows the dilatational wave front towards the impact direction. Measuring the crack tip position in the 3^{rd} and 4^{th} frames, it is estimated that the crack travels at about 2000 m/s, nearly equal to the dilatational wave speed in Homalite-100. It appears that this is not crack growth in the usual sense, and the stress concentration associated with a crack tip singularity is not observed ahead of the overall crack (compare with the isochromatics for subsonic and intersonic shear crack growth shown in Fig. 3.2). Post-mortem examination of the features of the fracture indicate the sequence of events: Fig. 3.6 shows a close-up view of the specimen in the region indicated by the dotted rectangle in Fig. 3.3; periodically spaced cracks, oriented at an angle to the plane of the groove are clearly seen. These are reminiscent of the echelon cracks observed in rock fracture under shear loading. Further details of these cracks can be seen in Fig. 3.7, where a scanning electron microscope image of the fracture surface is shown. Both of these images reveal that crack growth on the trapped groove plane is really a sequence of nucleation of cracks

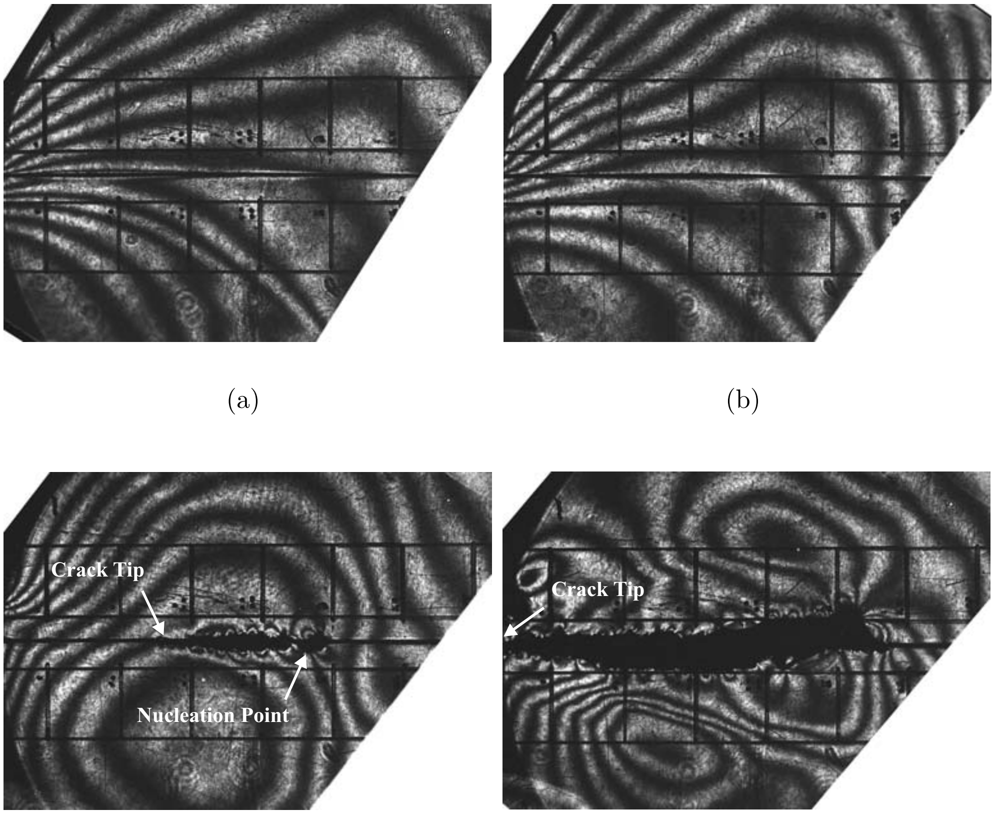

(a) (b)

(c) (d)

Figure 3.5: Nucleation and growth of an intersonic shear crack in a Homalite-100 specimen. Frames are at $11\mu s$ time interval. Square grid is 10 mm to a side.

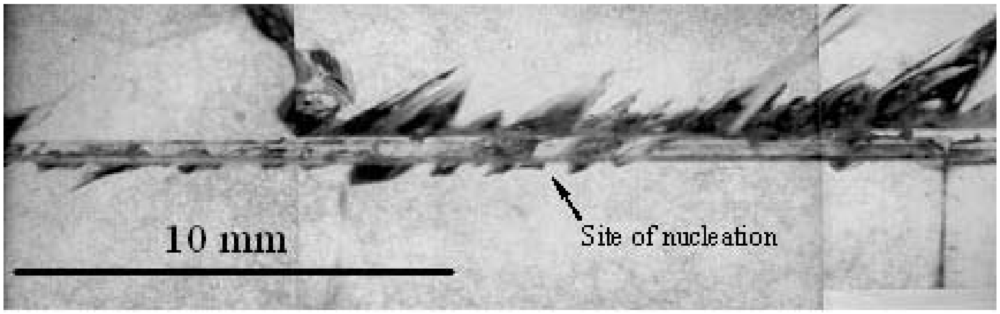

Figure 3.6: Formation of echelon cracks across the plane of the groove.

oriented at an angle to the groove plane. With this mechanism in mind, if the isochromatics in the 3^{rd} frame of Fig. 3.5 are again examined closely, one can observe that each one of the nucleated crack shows a concentration of isochromatic fringes indicating the multiple crack tips which is shown in Fig. 3.8. This sequential nucleation and coalescence of such echelon cracks is similar to the daughter crack mechanism suggested by Andrews [3] for the transition from the sub-Rayleigh shear crack to intersonic crack speeds. However, in the present case, we see that the successive nucleation is directly in the intersonic range and there is no crack that transitions from subsonic to intersonic speed in this case.

When the impact speed is increased to the range of 40 m/s, the shear stress induced along the plane of the groove upon impact is large enough to trigger crack initiation from the impact end. An example is shown in Fig. 3.9 for a Homalite specimen; in the first $50\mu s$, the propagation of the stress wave loading from the impact end to the right side can be seen; the dilatational wave speed can be determined from the sequence to be 2000 m/s. At the

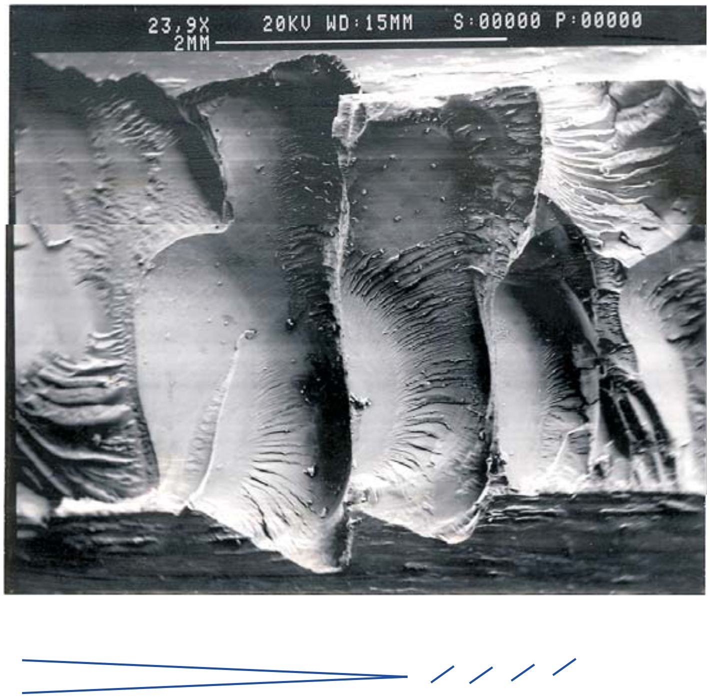

Figure 3.7: High resolution scanning electron microscope image of the fracture surface showing the details near the crack nucleation site. The serrated surface feature indicates multiple nucleation of echelon cracks at an angle to the groove plane that coalesce to form the shear crack as suggested by the sketch below the photograph.

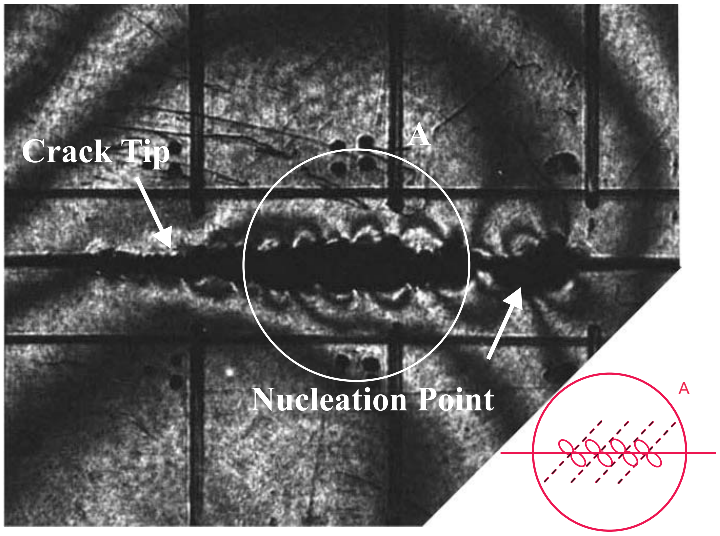

Figure 3.8: One frame from a high speed sequence showing a concentration of isochromatic fringes which indicate the multiple crack tips.

6^{th} frame, distortions in the fringe patterns can be seen at the left end of the image; this is the result of nucleation of a crack at the groove plane near the impact end. This pattern gets well organized in the subsequent two frames and one can then clearly observe a disturbance propagating along the plane of the groove at a speed of $v = \sqrt{2}C_s$; that the groove plane is fractured behind this disturbance can be verified by observing the echelon cracks visible in the last frame of Fig. 3.9. Post-mortem examination of the fracture surface indicated that the mechanism of echelon crack formation was identical to the case of lower impact speed. Clearly, the crack appears to grow at a speed of $v = \sqrt{2}C_s$ in this homogenous material. However, the fringe patterns are quite unlike the ones calculated from the asymptotic field and bring to question the dominance of the asymptotic field in Eqs. (3.9) and (3.10) in the vicinity of

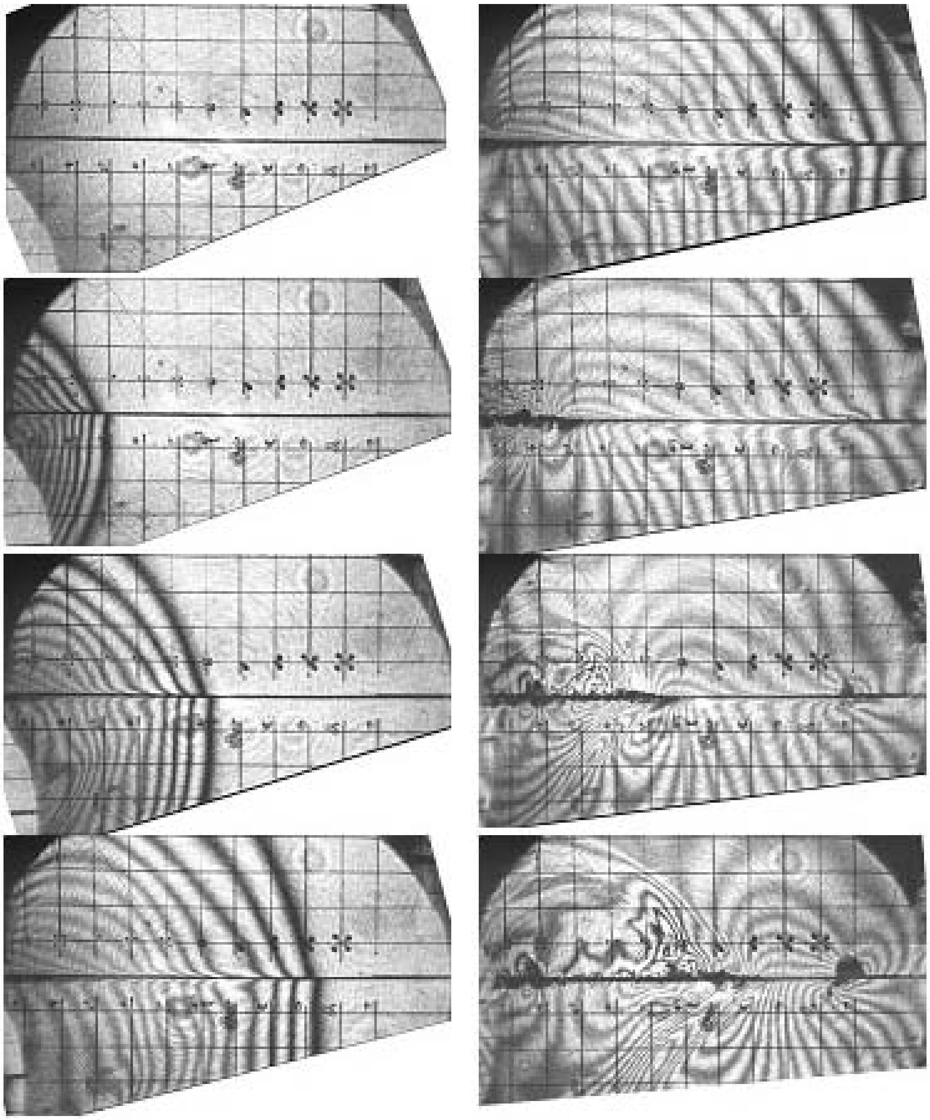

Figure 3.9: Nucleation and growth of an intersonic shear crack in a Homalite-100 specimen. Frames are at $10\mu s$ time interval. Square grid is 6.35 mm (0.25 in) to a side.

the crack tip. Furthermore, for a crack propagating a $v = \sqrt{2}C_s$, if the process region is small, one should not observe propagation of disturbances from the crack tip with the shear wave speed into the bulk of the material. The clear presence of the moving shear disturbance can be identified by the differences in the fringe densities and the discontinuities the fringe patterns suggests that the process zone must be quite large; the fact that echelon cracks are nucleated at large distances (of about 0.5 mm) indicates that the fracture process region is so large that the asymptotic field may have very little dominance.

3.4 Numerical Simulation of Mode II Loading

We now turn to a simulation of the dynamic experiment where the echelon cracks are nucleated. For comparison with experimental results, we perform the 3D finite element simulation. In the finite element simulation, the pressure loading measured from the current data of the Rogovski coil with the peak magnitude of about 35.6 MPa is applied to the Homalite-100 specimen. As discussed in Section 3.3, the nucleation of the echelon crack occurs at the point where the incoming shear wave meets the reflected dilatational wave. The large increment in the shear stress along the groove that occurs at this time will drive the crack initiation and growth. In order to determine the stress evolution, one element located in the center of the groove at the anticipated nucleation position is selected. As we expect, the shear stress level of the specimen at a position inside the groove is higher than the stress level of the specimen at the position outside the groove depending on the depth of the groove. In our simulations, the ratio of w/w_1 (indicated in Fig. 3.3) is 2.7. In the experimental results on shear crack shown in Fig. 3.10, the angle of the echelon cracks to the groove plane can be measured directly from the experimental specimen. The measured angle shown in Fig. 3.10 is 40° approximately. This result can be compared with the calculated angle from the stress components at the anticipated location of the nucleation of echelon cracks along the inside groove in simulation. The stress variations inside the groove at a position 67 mm away from the loading part are shown in Fig. 3.11. In this figure, the time variation of stress components σ_{11}, σ_{22}, σ_{12} as well as the principal stress σ_1 are shown. The orientation of the maximum principal stress is shown in Fig. 3.11 (b). The P-wave corresponding to the edge loading arrives at about 28 μs and generates a compressive stress of about 25 MPa. Large shear stresses are also generated within the groove (as expected from the experimental observations). The interation between the reflected P-wave and the incoming shear wave occurs at this location at about $65 \sim 70$ μs. Corresponding to this time, there is a sharp increase in the tensile principal stress causing nucleation of echelon cracks normal to this principal stress. The calculated angle of the echelon cracks to the groove plane based on the failure along the plane of the maximum tensile stress is 40° approximately and the corresponding tensile stress is about 27 MPa at about 68 μs. This is consistent with the angle of the echelon cracks measured in experiment shown in Fig. 3.10.

In summary, experiments on shear loaded specimens, with grooves to

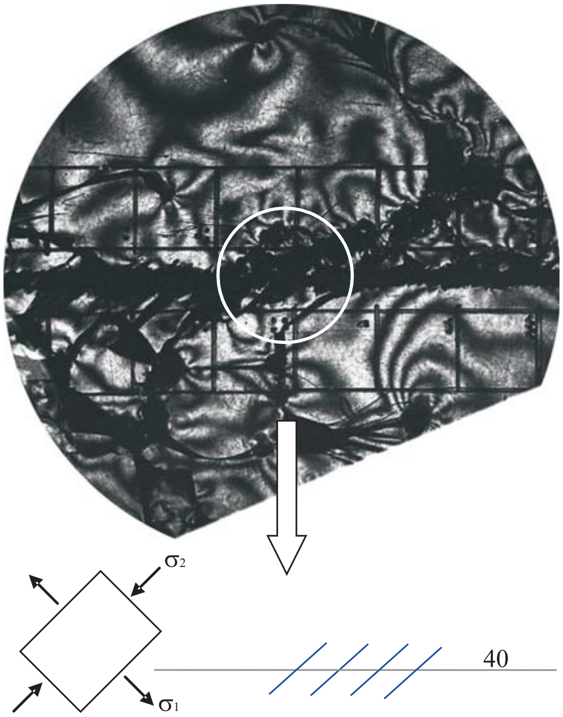

Figure 3.10: One frame from a high speed sequence showing the nucleation of the multiple echelon cracks in a Homalite-100 specimen.

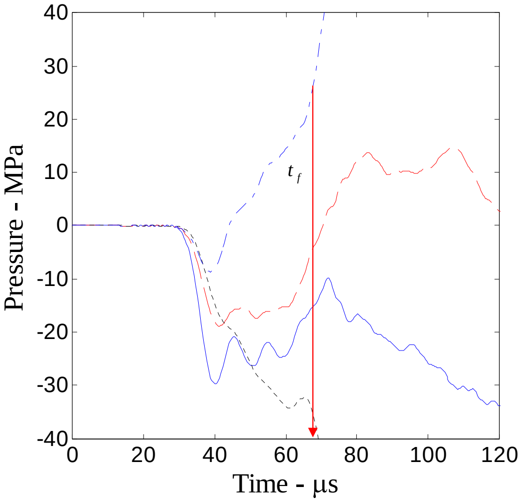

(a)

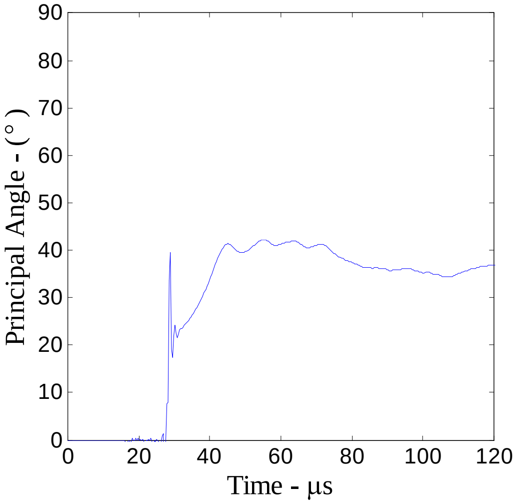

(b)

Figure 3.11: Variation of the calculated (a) stresses at a point inside groove in simulation. σ_{11}, σ_{22}, σ_{12} and σ_1 are represented by the solid blue line, dashed red line, dotted black line and dash-dot blue line respectively; (b) principal angle β.

trap the crack to grow under mode II symmetry within the plane of the groove, indicate that shear cracks can grow at speeds in the intersonic regime, with the nucleation and coalescence of the echelon cracks being the main mechanism of fracture. This observation supports a conjecture by Craggs [17], that there should be no limit to the crack speed in principle, because fracture would occur instantaneously everywhere if the entire prospective crack plane could be brought to the critical state; we have accomplished this in the present example by the concentration of shear stress in the groove generated at the speed of the dilatational wave. Numerical simulation shows that the echelon cracks are well aligned perpendicular the maximum principal (tensile) stress generated in this specimen. The spacing is interpreted as an intrinsic characteristic of the failure process. These experiments also enable the determination of the dynamic failure stress at which microcracks are nucleated.

Chapter 4

Frictional Sliding under Dynamic Loading

The existence of a slip pulse along the frictional interface under dynamic loading is evidence of dynamic slip. The possibility of two identical half-spaces sliding with friction due to the presence of separation waves and/or stick-slip waves was studied by Comninou and Dundurs [13–15]. Nosonovsky and Adams [36, 37] studied the sliding of an elastic half-space against another elastic half-space and showed that steady sliding is compatible with the formation of a pair of body waves (a plane dilatational wave and a plane shear wave) in each elastic body radiated from the sliding interface. Each wave moves at a different angle with respect to the interface such that the trace velocities along the interface are equal and supersonic. Although it has been shown that a solution in the form of waves radiated from the contact interface can exist, the origin of these waves has not been addressed. Adams [1] investigated the sliding of two dissimilar elastic bodies due to periodic regions of slip and stick propagating along the interface. The results of Adams show that a slip pulse travels through a region which otherwise sticks. In more recent works, Adams [2] investigated the propagation of a slip pulse of the same nature traveling with an intersonic speed and demonstrated that such a pulse can exist for sufficient friction and for modest mismatches in material combinations. However, few experimental results are available; Rosakis [49] has recently shown that frictional slip across interfaces with a quasi-static pre-stress can also grow into the intersonic regime.

4.1 Plane Wave Impinging on an Interface

In this section, we focus on frictional slip under compressional planar waves which occurs at different sliding velocities - in the range from a few μm/s to a few hundred m/s. Our interest is in the high end of the speed range, when slip occurs across the interface at speeds comparable to the elastic wave speeds in the material. To do this, a novel apparatus has been constructed for the study of friction under such extremely high rates of loading. Essentially, the stress state across a frictional interface is brought to the critical state behind the dilatational wave. If slip occurs across the interface, it will be forced to run along the interface at this speed. Through variation of the quasi-static or dynamic pre-stress on the frictional interface, and through variation of the stress pulse, the approach to criticality can be altered almost at will.

4.1.1 Experimental Configurations for Mixed-Mode Loading on Frictional Interfaces

The electromagnetic loading scheme described in Chapter 2 was modified to delve into the fundamentals of dynamic friction. Two polycarbonate plates with 300 mm × 100 mm (12" × 4") in 2-D dimensions and thickness of 5.6 mm (0.25") are machined to have an interface at an angle α as illustrated in Fig. 4.1. The interface is preconditioned by abrading with a sand paper (a systematic variation of this parameter has not yet been explored) in order to evaluate its frictional characteristics. The two specimen plates may be made either of the same material or of different materials, generating different frictional characteristics. A static preload below the slip threshold may be applied through a load frame; alternatively, a dynamic stress can be superimposed through a stress wave generated from a second electromagnetic loading system. A flat copper strip is folded back on itself or wrapped into a coil with the space between the layers filled with an insulator such as mylar. This assembly is then introduced at the bottom of the specimen plate as indicated in the schematic diagram in Fig. 4.1. For typical coils used in our experiments, the crack surface pressures are in the range of 1 MPa to 1 GPa. Variation of the angle α can be used to alter both the ratio of the shear stress to normal stress in the loading pulse as well as to alter the projected velocity of the loading wave along the interface. Essentially, the loading of the interface occurs at the velocity $C_d/\sin\alpha$ as this is the speed with which the dilatational wave sweeps along the frictional interface. We note that this loading configuration is equivalent to an infinite plate, with a well characterized stress state behind the dilatational wave for the duration of the current pulse; hence this represents a *clean* experiment where the input conditions are clearly identifiable.

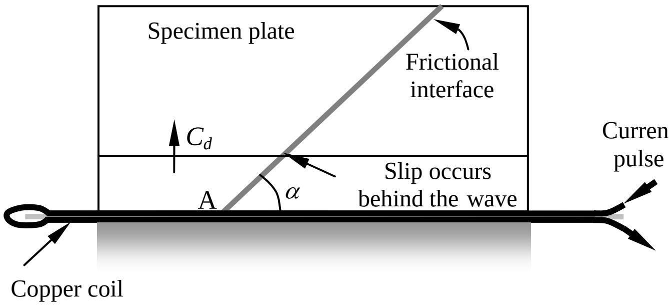

Figure 4.1: Scheme for dynamic friction characterization.

4.1.2 Propagation of a Slip Pulse and Stress Variation along Frictional Interface

Two different experimental results corresponding to two different angles ($\alpha = 45^o$, $\alpha = 60^o$) are described here. For the plane wave (with a magnitude of 40 MPa) impinging at an angle $\alpha = 45^o$ on a frictional interface, the development of frictional sliding is indicated in four frames selected from this experiment as shown in Fig. 4.2. In this particular experiment, due to inadvertent misalignment, the two faces did not contact each other along the entire length of the interface and the initial loading occurred only on the bottom half of the specimen; nevertheless, the results are illuminating in understanding the development of sliding. The dilatational wave front is identified in the frame at 28 μs shown in Fig. 4.3 by the blue line. In the bottom half of the specimen this wave encountered a traction free surface instead of a frictional interface; hence, two waves - a dilatational wave and a mode-converted shear wave - were reflected from the free surface. Elastodynamic wave theory indicates that the amplitude of the reflected dilatational wave is small and hence is not visible in the isochromatic fringe pattern. The reflected shear wave is clearly identified in Fig. 4.3

The result of this process of reflection is that the gap between the two halves of the plates is now closed with an unknown contact pressure; the surfaces may now slide frictionally if sufficient shear stress is imposed. The imperfect contact between the two halves of the plate resulted in the generation of a shear wave at the point A indicated in Fig. 4.1. This shear disturbance generates slip across the line of contact between the two halves of the plate; tracing the speed of propagation of the isochromatics into the specimen, it is easy to identify that a shear disturbance is traveling into the specimen, while this drives a slip to grow along the interface at a speed of about 1250 m/s; this is precisely $C_s/\sin\alpha$ for the polycarbonate specimen.

To demonstrate this conclusively, this experiment was repeated with $\alpha = 60^o$ and four frames from the sequence of images from this experiment is shown in Fig. 4.4. The isochromatic fringes show very clearly that the shear Mach waves (marked in the frame at 39 μs) make an angle of $\alpha = 27.1^o$ with respect to the interface suggesting that slip is triggered along the interface right behind the dilatational wave. The measured speed of this disturbance along the frictional plane is 1900 m/s; once again, this matches the estimate based on $C_s/\sin\alpha$; these results are Table 4.1. Thus, the frictional sliding occurs right behind the shear wave that travels with this projected velocity along the interface.

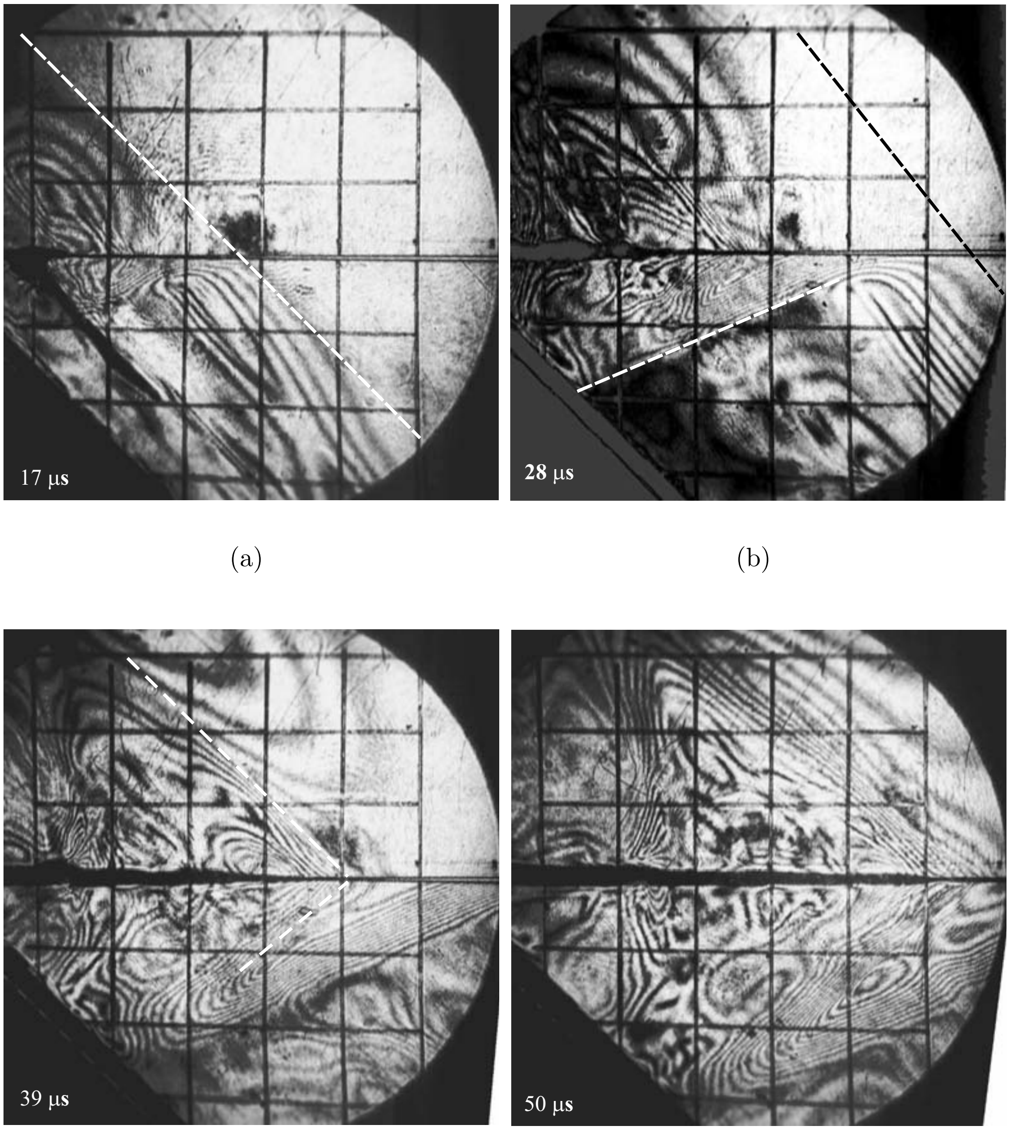

(a) (b)

(c) (d)

Figure 4.2: Sequence of high speed images of a plane wave propagating at an angle of 45^o with respect to the interface between two polycarbonate plates. Square grid is 10 mm to a side; frames are 11 μs apart in time.

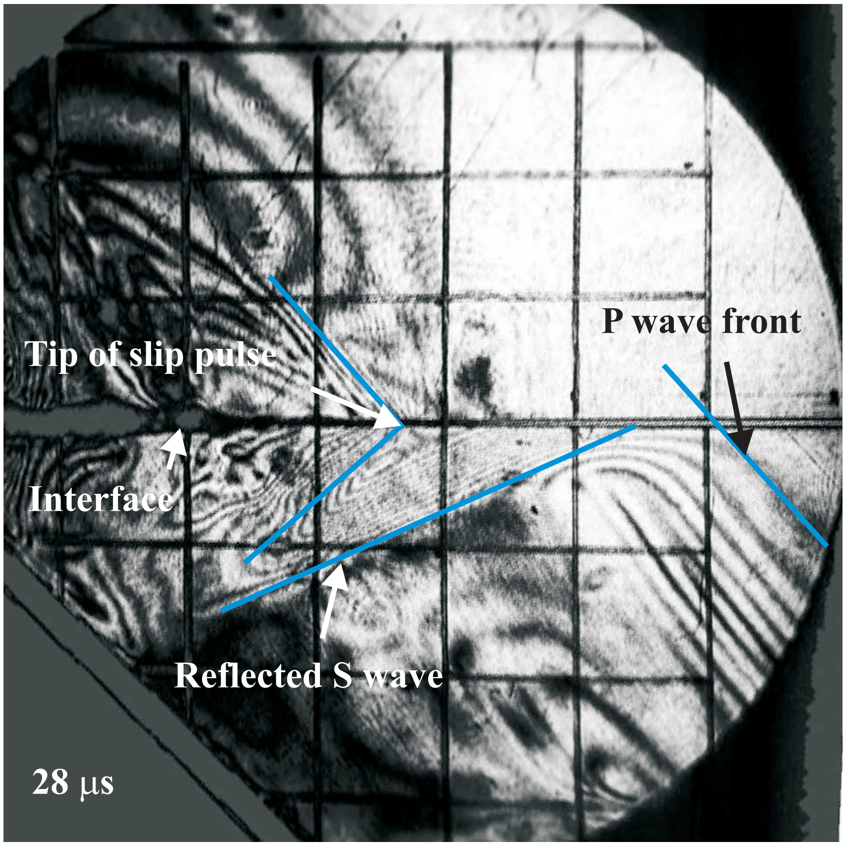

Figure 4.3: One frame from a high speed sequence indicating the effect of a plane wave propagating at an angle of 45^o with respect to the frictional interface between two polycarbonate plates. The shear Mach wave is easily identified.

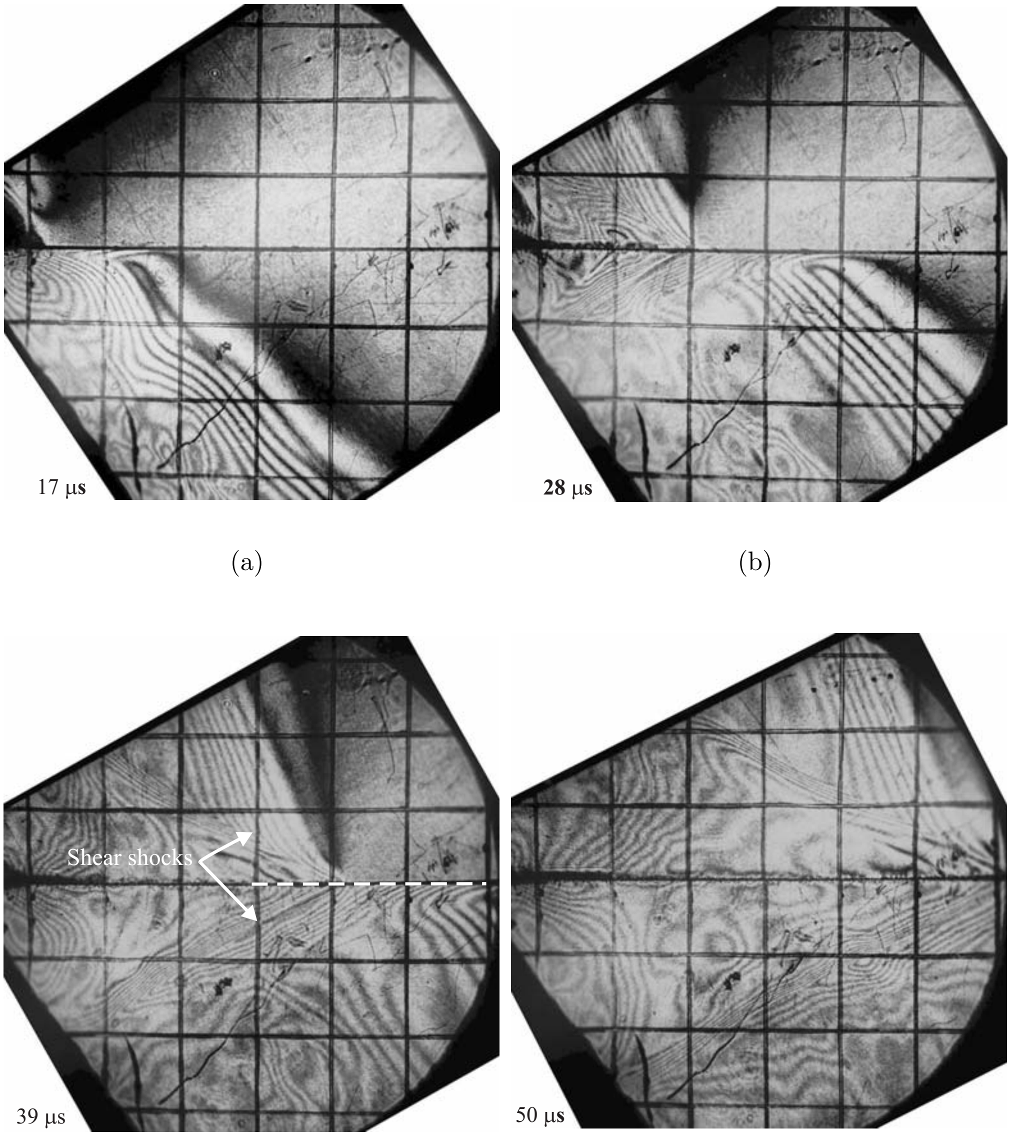

(a) (b)

(c) (d)

Figure 4.4: Sequence of high speed images of a plane wave propagating at an angle of 60^o with respect to the interface between two polycarbonate plates. Square grid is 10 mm to a side; frames are 11 μs apart in time.

For both inclination angles of the interface stress singularity characteristic of the intersonic crack is not observed, but simply a steady build-up of shear stress until slip occurs. This is very similar to the case of the shear cracks discussed in Chapter 3. For frictional interfaces with the same material on either side, the isochromatics may be interpreted directly in terms of the shear stress along the interface. Counting the order of fringes from before the primary loading through the reflections and the slip, the variation of the shear stress along the line marked in Fig. 4.5 was obtained and is shown in Fig. 4.6. The shear stress is seen to build-up gradually to a maximum (of about 10 MPa) at the leading edge of the slip pulse and to decay rapidly over a 5 mm length; this is the zone over which slip occurs. Note that this may not be a self-sustaining slip event, but driven by the shear wave. However, this measure of the state of the interface is incomplete since one must augment the measurement with a characterization of the slip speed across the interface. This remains a great challenge for photomechanics; perhaps dynamic moiré or digital image correlation method coupled with dynamic photoelasticity could provide the answer.

Table 4.1: Properties of a slip pulse.

Test ♯		Polycarbonate	Speed Range
	Mach wave angle	43.5°	
Test 1	v/C_d	0.71	Intersonic
	v/C_s	1.45	
	Mach wave angle	27.1°	
Test 2	v/C_d	1.1	Supersonic
	v/C_s	2.2	

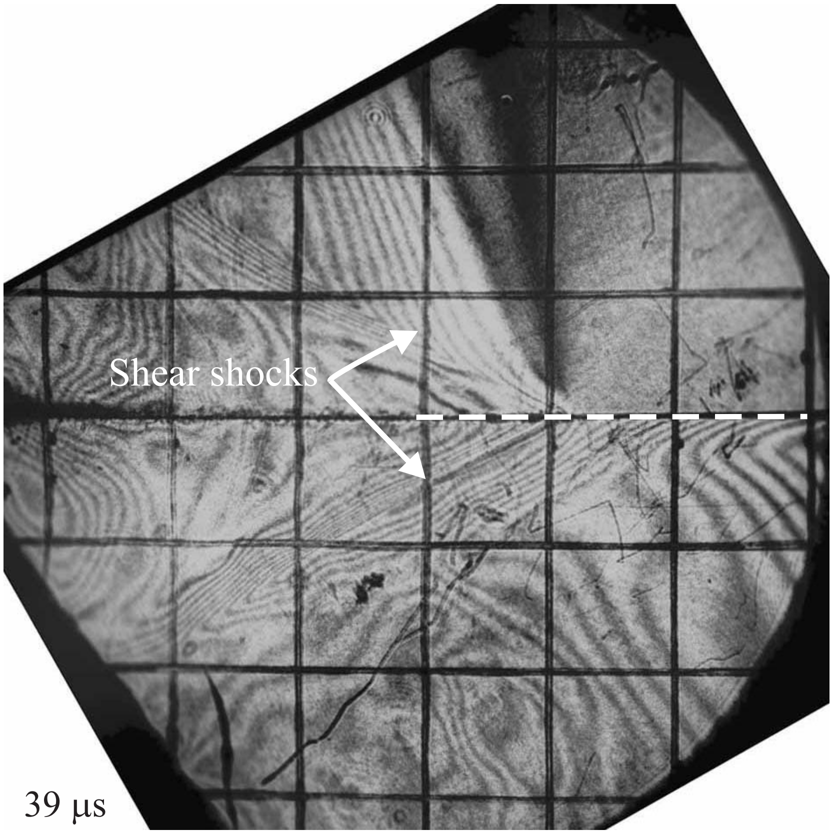

Figure 4.5: One frame from a high speed sequence indicating the effect of a plane wave propagating at an angle of 60^o with respect to the frictional interface between two polycarbonate plates. The shear Mach wave is easily identified. The dotted line indicates position along which the shear stress displayed in Fig. 4.6 was evaluated.

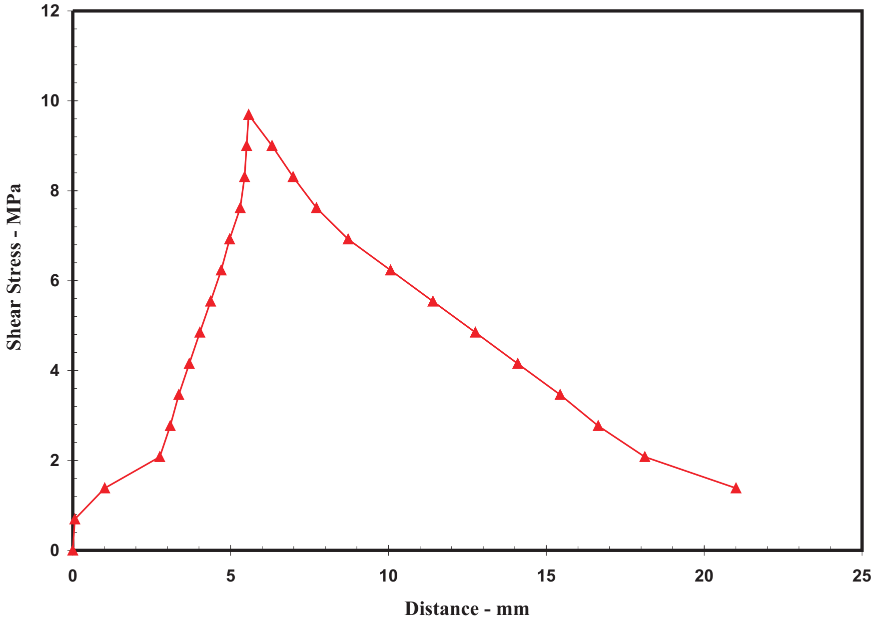

Figure 4.6: Variation of the shear stress in the slip zone evaluated from the isochromatics indicated in Fig. 4.5.

4.2 Cylindrical Wave Impinging on an Interface

In this section, we focus on the frictional slip under compressional cylindrical wave which occurs at different sliding velocities. This implementation of the loading scheme is more amenable to the study of nucleation of slip. In experiments reported here, we use polycarbonate and Homalite-100 plates; these materials are birefringent and hence we used dynamic photoelasticity to record isochromatic fringe patterns. The loading scheme is described below.

4.2.1 Experimental Configurations for Mixed-Mode Loading on Frictional Interfaces

A new experimental configuration whose purpose is to generate the dynamic slip along the material frictional interface and find the conditions under which dynamic slip initiates is shown in Fig. 4.7. A Polycarbonate plate with 400 mm × 150 mm (16" × 6") in 2-D dimensions and thickness of 9.5 mm (3/8") for bottom plate and a Homalite plate with 400 mm × 100 mm (16" × 4") in 2-D dimensions and thickness of 4.8 mm (3/16") for top plate are used. The two plates are aligned along the interface and held in a specially designed fixture to remove the gap of the interface. In this arrangement, a semicircular cut-out is made in a large plate and the coiled copper strip is inserted into the gap between the cut-out as illustrated in the figure. Upon discharge of the current through the copper coils, the electromagnetic repulsion generates a cylindrical stress wave, whose wavefront is illustrated in the figure. Behind the wavefront, of course, the load amplitude increases over time as indicated in Fig. 2.3. This cylindrical stress wave interacts with the planar frictional interface, again with a possible compressive static prestress. Since the angle between the compressive wave and the interface varies continuously, the ratio of the shear stress to normal stress increases along the interface; at some critical angle (one that depends on the frictional characteristics of the interface), slip or interface cracking will nucleate (initiate) and move along the interface. Furthermore, since the projected velocity of the wave along the interface increases continuously, and is larger than the dilatational velocity, conditions along the interface can be altered more rapidly than in other kinds of experiments.

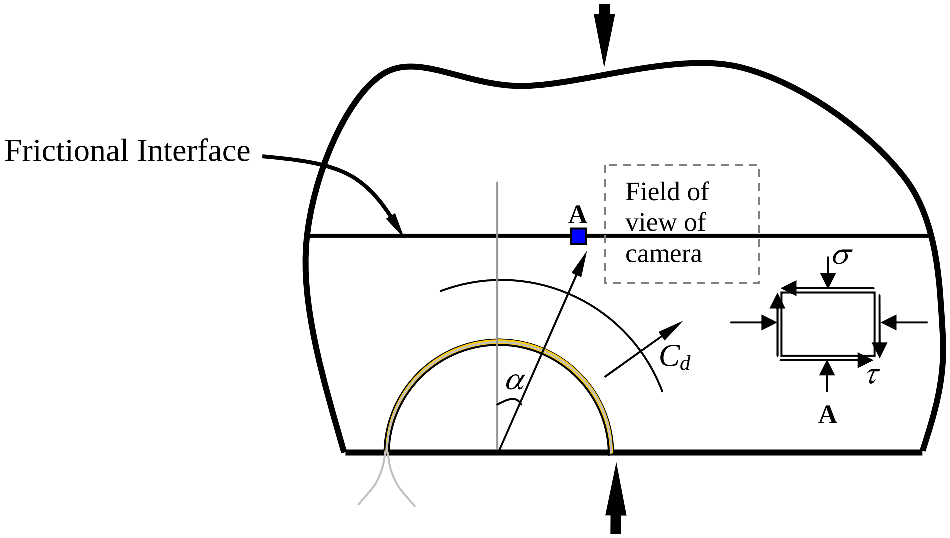

Figure 4.7: Scheme for dynamic friction characterization; cylindrical wave approaches a frictional interface. The velocity of the wave along the interface increases with the angle α. At the critical angle α_{cr}, slip is nucleated and may propagate along the interface.

4.2.2 Initiation and Propagation of a Slip Pulse along Frictional Interface

Some experimental results from the impingement of a cylindrical wave on a frictional interface are presented here. In this experiment, a Homalite plate was placed on top of a polycarbonate plate. A cylindrical wave was generated using the arrangement shown in Fig. 4.7 in the polycarbonate plate and made to arrive at the interface. A sequence of images is shown in Figs. 4.8 and 4.9 corresponding to the different range of angles α under a cylindrical wave of amplitude 40 MPa. Fig. 4.8 shows the isochromatic fringe patterns obtained with the range of the inclination angle $14^o < \alpha < 32^o$. The cylindrical compressive loading wave (P wave) front propagates from the bottom. The initiation location of a slip event is not clear because the stress state in this inclination angle range is not enough to drive a slip.

Fig. 4.9 shows the experimental results with the range of the inclination angles $32^o < \alpha < 45^o$ while the loading pressure was 40 MPa. The arrival of the cylindrical wave front within the field of view of the camera is indicated in the first frame. In the following frame (11 μs later), the wave front must have passed across the interface and into the Homalite plate; however, fringes are not observed in the Homalite. We believe that this is because at early times, the normal stress and shear stress passing through the interface (caused by the weight of the specimen and the early loading) are small and the slip threshold is quite low. Since the fringe sensitivity of Homalite is also quite low, fringes are not visible. In the 3rd and 4th frames, the shear stress builds up in amplitude

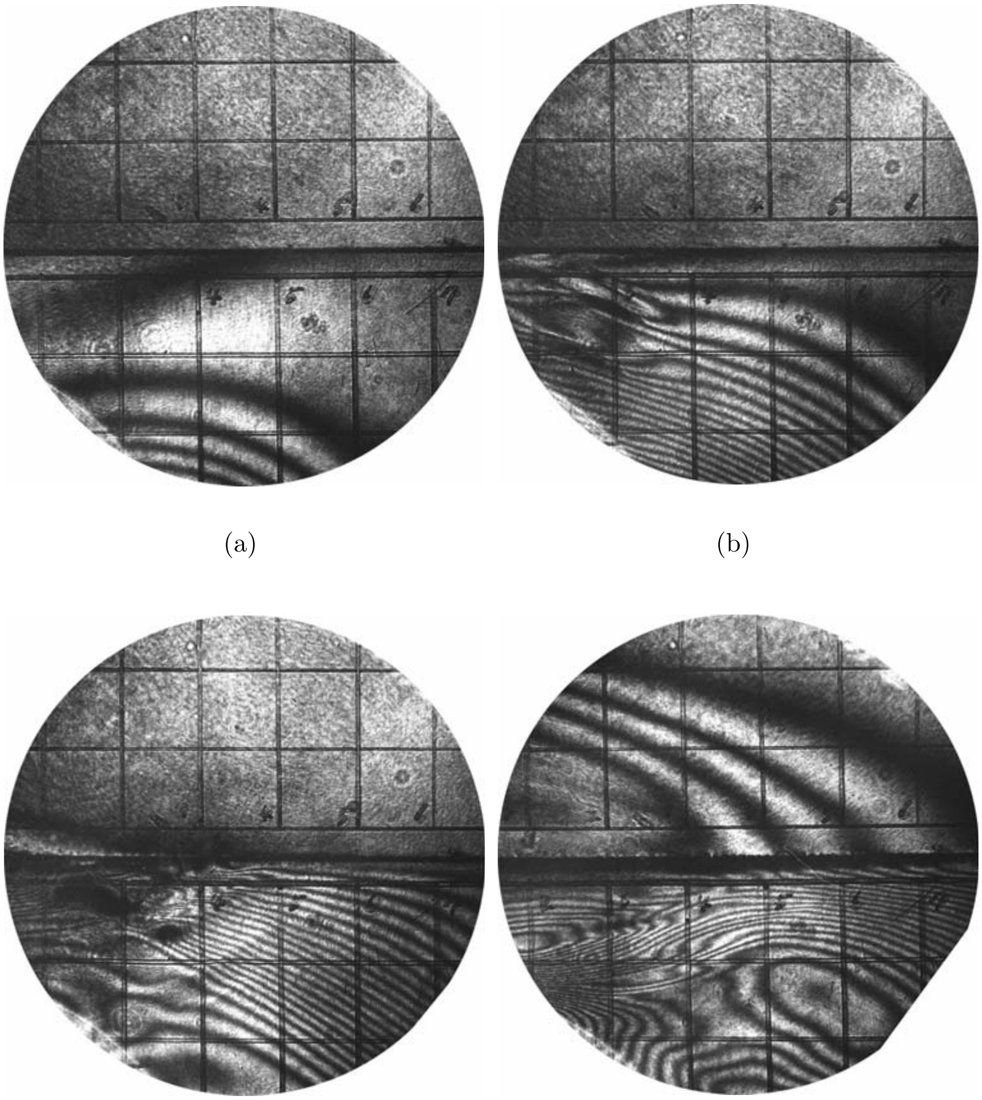

(a) (b) (c) (d)

Figure 4.8: Isochromatics from a cylidrical wave impinging on an interface between a polycarbonate and Homalite-100 specimen (2.25" field of view, $14^o < \alpha < 32^o$, frames are $11 \mu s$ apart).

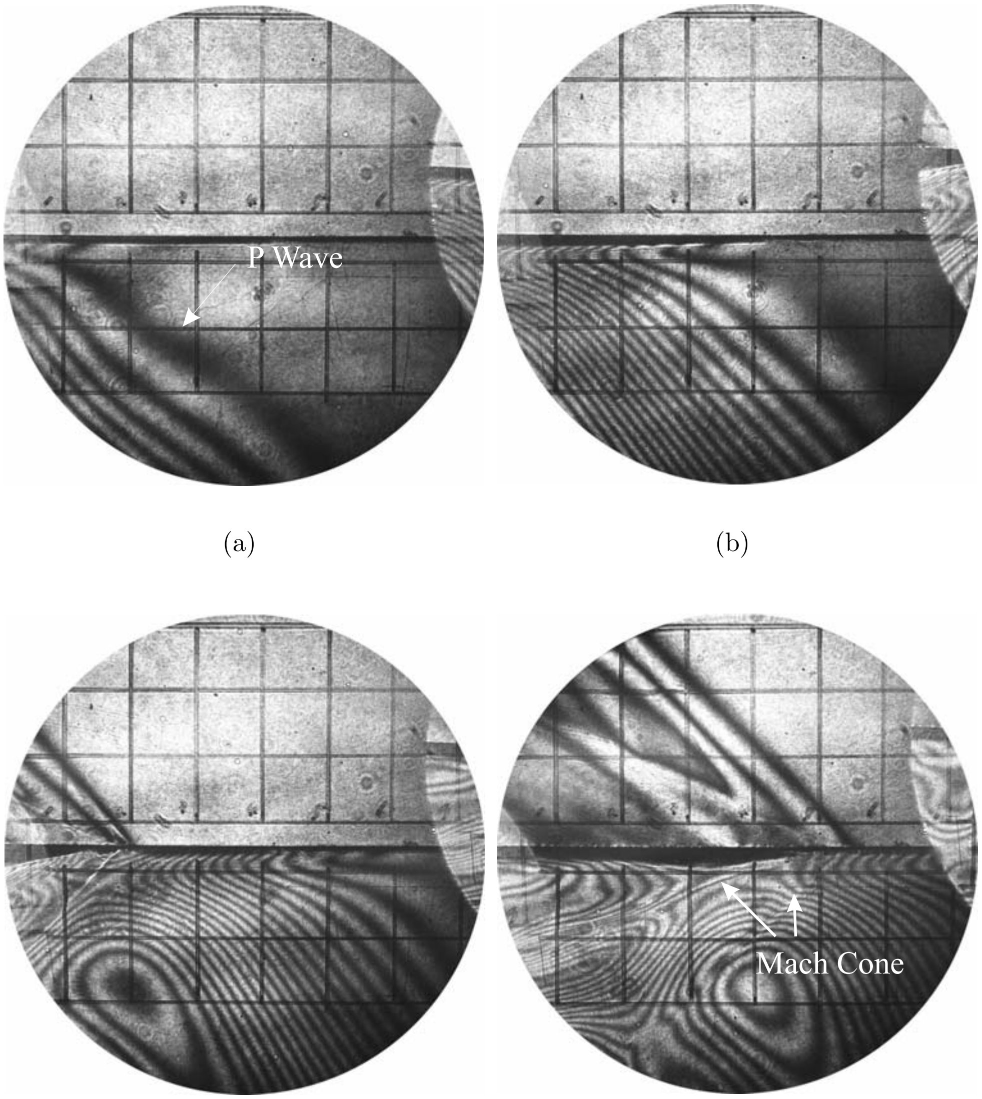

(a) (b)

(c) (d)

Figure 4.9: Isochromatics from a cylidrical wave impinging on an interface between a polycarbonate and Homalite-100 specimen (2.25" field of view, $32^o < \alpha < 45^o$, frames are $11\mu s$ apart).

and a few fringes become visible in the Homalite plate. The propagation of the disturbance along the interface can be clearly seen (marked in the photograph as the arrow). Direct measurement of the position of the disturbance of along the interface from the high speed images results in a speed of 3030 m/s which corresponds to $v = 1.34\ C_d$ with respect to the Homalite and $v = 1.44\ C_d$ with respect to the polycarbonate; these correspond to supersonic propagation of the sliding event along the interface. Hence, one should expect two sets of shock waves, one corresponding to the dilatational wave speed and the other corresponding to the shear wave speed; these are marked by the red lines in Fig. 4.10 for easy identification. Based on slip propagating at a speed of 3030 m/s and the appropriate wave speeds, the predicted shock angles in the Homalite are 48^o and 23^o and in the polycarbonate side 44^o and 16.5^o for the dilatational and shear shocks respectively. These are within half a degree of the measured angles for the shock and are summarized in Table 4.2. Since the speed of the dilatational and shear waves is different in the two materials, the shock angles in the two sides of the interface are different.

In summary, we present two different types of slip experiments. In Section 4.1, using a novel experimental model of applying dynamic loading

Table 4.2: Experimental results of the speed of the slip pulses.

Test ♯		Homalite-100	Polycarbonate	Speed Range
	Mach wave angle	48°	44°	
		23°	16.5°	
1	v/C_d	1.35	1.44	supersonic
	v/C_s	2.56	3.52	

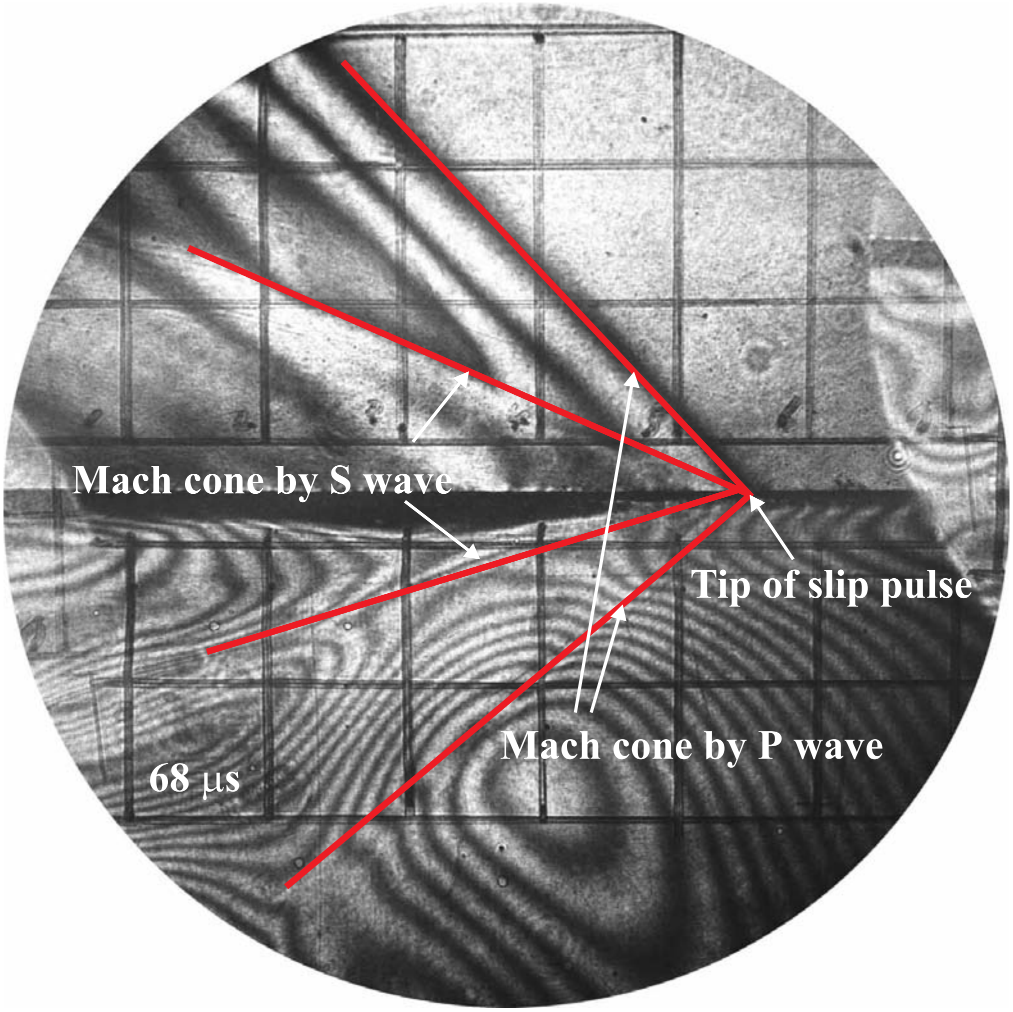

Figure 4.10: One frame from a high speed sequence indicating the effect of a cylidrical wave impinging on an interface between a polycarbonate and Homalite-100 specimen. Mach waves corresponding to the dilatational and shear waves are identified by the red lines.

on frictionally held interfaces, we obtained several interesting results for a slip pulse due to frictional sliding. We presented a slip pulse propagating at a speed of intersonic range or close to supersonic. This is done by controlling the inclination angle α. The isochromatic fringe patterns showing the shear stress along the sliding interface were presented. The shear stress is seen to build up gradually to a maximum of about 10 MPa at the leading edge of a slip pulse and to decay rapidly over 5 mm slip length.

In Section 4.2, we present the experimental results on the dynamic slip at an interface brought to the critical state behind the dilatational wave. Under proper conditions, the slip pulses due to the dynamic slip event initiate and propagate along the interface at speeds faster than the wave speed of the materials. From these results, the approach to critically can be altered almost at will through variation of the inclination angle on the frictional interface, and through variation of the dynamic loading. Since the dynamic isochromatics did not indicate any characteristic features of the mode II intersonic singular stress field, it is difficult to extract quantitative information on the crack speed versus the driving force. Further studies with additional diagnostic tools that can measure particle velocities may need to be used to quantify the energy dissipation during intersonic crack growth in homoneneous materials. A new experimental method aimed at providing all dynamic stresses and principal angle β was developed in this study and is discussed in Chapter 5.

Chapter 5

Dynamic Measurement of Two-Dimensional Stress Components in Birefringent Materials

In this chapter, we adopt classical methods of photoelasticity and Mach-Zehnder interferometry in a new combined arrangement in order to determine both principal stresses and their orientations simultaneously. The method is equally applicable to static and dynamic problems. In dynamic problems the measurement may be made with high-speed photodetector at very high temporal resolution at a single point or a small array depending on the detector array and recording device; this eliminates the need for high-speed photographic system, but more importantly provides complete, time-resolved evolution of all stress components. Examples of application of the method are demonstrated.

Photoelasticity has been viewed as a full-field optical method for stress analysis ever since the discovery of stress-induced birefringence by Brewster nearly two centuries ago. However, a significant limitation of the method is that it only provides the principal stress difference when used in a circular polariscope. The principal stress orientation can be determined in a linear polariscope, but this requires multiple measurements, with different orientations of the polarizer; this is quite tedious and in modern applications, this approach is rarely used. Many major contributions have been made by numerous investigators towards extraction of the complete stress field. In particular, Favre [22] and Post [41] combined photoelasticity with optical interferometry to separate determine the two principal stresses independently. Others, such as Tardy [55], suggested modifications to the circular polariscope in order to be able to extract partial fringe orders. Nevertheless, the method of photoelasticity has been used primarily as a technique for the evaluation of the principal stress difference; this measurement is then augmented with some analytical or numerical model in order to extract quantitative stress information from the specimen. In this chapter, we present a combination of Favre and Tardy in an arrangement that provides complete determination of the two-dimensional stress components.

Phase shifting photoelasticity has been studied recently by numerous researchers [5, 29, 35, 39]. The main idea behind the phase shifting methods is to acquire multiple images with a known phase change introduced in the optical path that are in addition to the phase change caused by the stressed specimen; this is accomplished by introducing changes in the orientations of the quarter-wave plates, and/or the polarizers. An inversion scheme is then used to extract the relative phase change introduced by the specimen. Problems associated with unwrapping the phase in terms of the absolute phase make the determination of the principal stress difference and principal directions in the specimen difficult. Different strategies and algorithms have been used in the literature; Ramesh [43] presents a discussion of these methods.

The need for multiple settings of the polariscope and sequential acquisition of images or intensity data limit the use of these techniques to equilibrium problems. Yoneyama et al. [64] present an interesting alternative to multiple imaging by using the RGB signals from color images obtained in an elliptical polariscope. Since our main interest is in transient problems, these methods based on acquisition of multiple images with phase shifting cannot be used directly. Furthermore, these techniques still do not allow easy separation of the principal stress components since it only the principal stress difference that is obtained with photoelasticity. Here, we present a method that is based on simultaneously monitoring the time evolution of intensity and phase in multiple optical paths in order to reconstruct the stress state in the specimen. With the prevalence of inexpensive laser diodes, photovoltaic sensors and optical components, the method presented here is capable of providing stress data at a point at high temporal resolution. It is also possible to use this method to obtain stress components in quasi-static problems; in fact, in quasi-static problems, it is possible in principle, to obtain full-field information by using multiple digital cameras.

5.1 Experimental Arrangement

We restrict attention to a single point on the specimen and consider time evolution of stress at this point. The complete optical arrangement is indicated in Fig. 5.1. The optical path P1 corresponds to a standard circular polariscope and hence gives isochromatic data. In path P2, the light passes

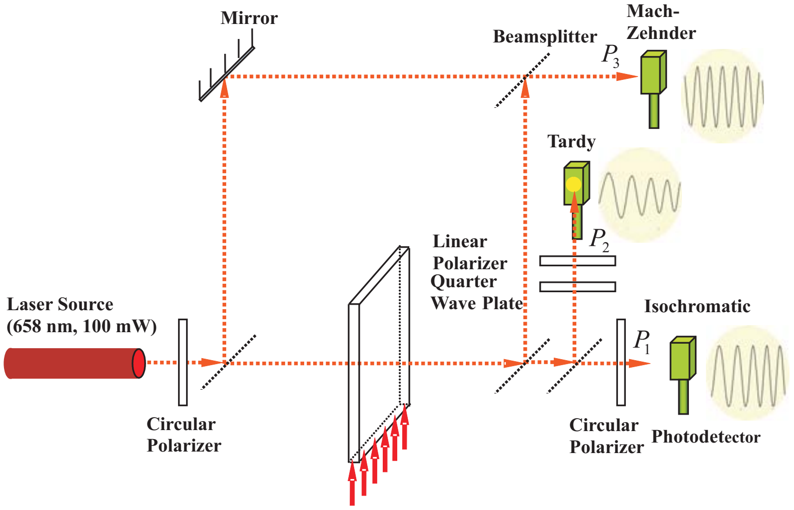

Figure 5.1: Schematic diagram for measurement of two dimensional stress components; the optical arrangement includes classical methods of photoelasticity and Mach-Zehnder interferometry implemented simultaneously.

through a circular polarizer, then the specimen, a quarter wave plate and finally a second polarizer oriented at an angle γ with respect to the axis; this corresponds to a variant of the Tardy compensation arrangement, but with fixed γ; this arrangement yields an intensity that depends both on the principal stress difference and the orientation of the principal axes. The last optical measurement corresponds to a Mach-Zehnder interferometer shown in Fig. 5.1 as path P3; the intensity variation obtained in this arrangement corresponds to the sum of the principal stresses. The light intensities observed in the three paths can be expressed as

$$I_{iso}(t) = k\cos^2[\Delta s(t)/2] \tag{5.1}$$

$$I_{Tardy}(t) = K[1 - \cos 2\gamma \cos \Delta s(t) - \cos 2\beta(t) \sin 2\gamma sin\Delta s(t)] \tag{5.2}$$

$$I_{MZ}(t) = 4a^2 \cos^2[\pi\delta(t)/\lambda] \tag{5.3}$$

where $\Delta s(t)$ the relative phase retardation and $\delta(t)$ the optical path length difference are given in terms of the stress optic law as:

$$\Delta s(t) = 2\pi h[\sigma_1(t) - \sigma_2(t)]/f_\sigma \tag{5.4}$$

$$\delta(t) = -h(n_0 - 1)(\sigma_1(t) + \sigma_2(t))\nu/E \tag{5.5}$$

$\sigma_1(t)$ and $\sigma_2(t)$ are the principal stress components, $\beta(t)$ is the orientation of the principal axis, h is the specimen thickness, and E and ν are the Young's modulus and Poisson's ratio respectively, n_0 is the unstressed refractive index of the specimen and f_σ is the material stress fringe value (see the Handbook of Experimental Mechanics for details of the derivation of the various light intensities).

We take $\gamma = \pi/4$ and hence the intensity in the Tardy arrangement can be simplified; with the measurements of the intensities along the three optical arrangements, we find $\Delta s(t), \beta(t)$ and $\delta(t)$

$$\Delta s(t) = 2\sin^{-1}[\sqrt{I_{iso}/k}] \tag{5.6}$$

$$\beta = \frac{1}{2}\cos^{-1}[\frac{1 - I_{Tardy}/K}{\sin \Delta s}] \tag{5.7}$$

$$\delta = \frac{\lambda}{\pi}\sqrt{I_{MZ}/4a^2} \tag{5.8}$$

We define $n(t) = \Delta s(t)/(2\pi)$ and $m(t) = \delta(t)/(2\pi)$ as the fringe order parameters in the isochromatic and Mach-Zehnder arrangements, but not restricted to integer values. The resolution of partial fringe orders really depends on the measurement resolution of the light intensity. Note that the fringe order parameter may be positive or negative depending on whether the principal stresses are tensile or compressive. Extraction of the absolute values of the principal stress components requires the signs to be estimated independently. Eq. (5.6) yields the principal stress difference, but with a phase ambiguity. However, in dynamic problems, we record the intensity at high temporal resolution, and therefore, identification of the absolute phase is simply a matter of counting peaks. Then Eq. (5.7) gives the principal orientation; however, since $\Delta s(t)$ varies rapidly in time as the stresses (and therefore the phase difference) build up, there is a rapid variation of $I_{Tardy}(t)$ that is similar to $I_{iso}(t)$, but nearly out of phase. On the other hand, one expects the variations in the principal orientations to be much slower in time (except possibly in the vicinity of wavefronts and Mach waves); therefore, one can extract the orientation of the principal directions by simply looking at the local maxima and minima of $I_{Tardy}(t)$. Setting $\Delta s(\tau) = \mp\pi$ at $t = \tau^{\pm}$ corresponding to maximum and minimum intensity, we get

$$I_{Tardy}^{max}(\tau^{+}) = K[1 + \cos 2\beta(\tau)], \quad I_{Tardy}^{min}(\tau^{-}) = K[1 - \cos 2\beta(\tau)] \tag{5.9}$$

This estimate indicates immediately that, if the minimum and maximum intensity from the Tardy signal do not vary significantly with time, then the principal orientations do not vary significantly as well. Therefore, the principal orientation can be determined using either Eq. (5.7) or Eq. (5.9). Finally, the Eq. (5.8) results in an evaluation of the sum of principal stresses, that once again must be interpreted by tracking the time variation of the fringe data in order to determine whether the thickness increases or decreases. We illustrate the application of this method with three examples. A photograph of the optical set-up is shown in Fig. 5.2; alignment of all the optical components is straightforward, but some aspects of the optical set-up require special attention. First, since a large number of optical elements are involved in the three different optical paths, a rather powerful laser-diode is needed; we use a 100 mW laser, powered by a 5V dc power supply (UH5-100G-658 Red Laser Diode Module, supplied by World Star Tech.). Second, care must be exercised in ensuring that the intensities of the two beams that make up the Mach-Zehnder interferometer are nearly the same in order to maximize fringe visibility; this is accomplished by using neutral density filters or partial mirrors at different positions in order to modify the light intensities appropriately.

Third, the beam diameter as it passes through the specimen is made to be

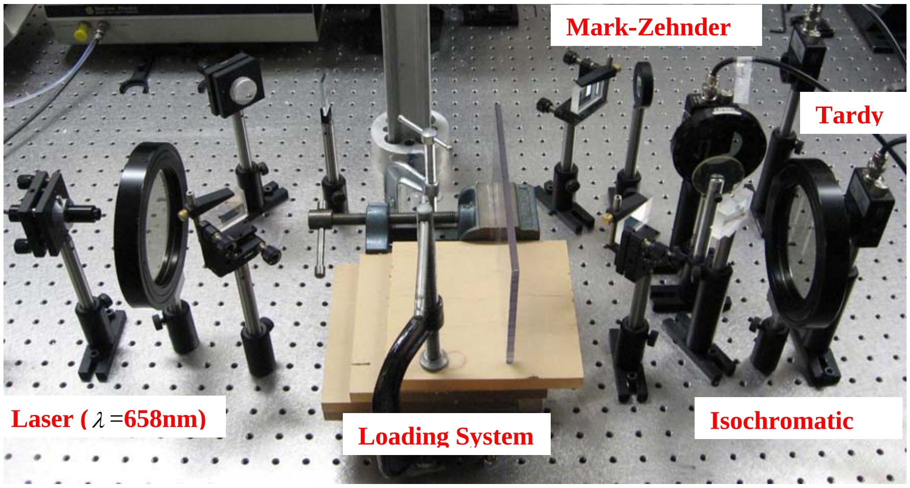

Figure 5.2: A photograph of the optical set-up for measurement of two dimensional stress componensts.

small since this determines the *gage* area over which the average stresses are measured. Fourth, the Mach-Zehnder beam, upon exit from the last beamsplitter is expanded so that, at least initially, the spatial extent of the interference fringe is of the order size of the detecting element. The light intensity variations were measured with a ThorLabs Model DET 10A detector. The sensor area is 0.8 mm^2. With a 50 Ω input impedance into the recording oscilloscope, a rise time of about 1 ns is obtained with this detector. However, the output voltage is rather low; peak-to-peak variations of five to ten mV is typically obtained in this arrangement; with the amplifiers set to high gains in order to monitor this low output, the signals are susceptible to high frequency noise. More powerful laser diodes may alleviate this problem a bit, but as we will show in the following, the signals are still easily interpreted by filtering out the high frequency noise.

5.2 Examples of Stress Measurement in Specimens under Dynamic Loading

Uniform Loading: We present three examples in this chapter, in order to validate the experimental method proposed here. We consider a plate with a uniform pressure loading along one edge as illustrated in Fig. 5.3 (a). Dynamic loading is accomplished with the electromagnetic loading scheme described in Section 2.1. The magnitude of the pressure varies as a function of time, depending on the time variation of the current pulse, as indicated in Fig. 5.3 (b). Thus a dynamic pressure load is applied on the specimen in the region over which the copper coil is pressed against the specimen. This loading scheme presents a simple uniaxial problem where the principal directions remain constant, at least during the first 150 μs of the test. The measuring scheme described above was used in this experiment, augmented with two independent measures of the field variation, in order to validate the new experimental scheme. The laser beam was pointed at a distance $d = 50$ mm from the loaded edge along the centerline of the specimen. The raw intensity signals obtained at this location from one experiment are shown in Fig. 5.4; the time reference should correspond to the beginning of load application along the left edge of the specimen, but an unresolved triggering error shifted the zero reference consistently by about $\tau_d = 20$ μs.

The signal from the Mach-Zehnder interferometer exhibited some zero-drift which has been corrected in the signal shown in the figure; also, a moving average filter has been applied in order to suppress high-frequency noise. Interpretation of the intensity data is quite straightforward. All three detectors are quiescent until $t_1 = d/C_d + \tau_d$ when the dilatational wavefront from the pressure loaded edge arrives at the point of observation and induces a sinusoidal change in the light intensity. It is apparent that the fringe number/order can be obtained simply by counting the number of peaks from the early stages of loading; fractional orders are resolved by identifying the phase of the cycle. At t_2 the presence of the corner of the plate will be felt at the observation point, but this has a minor influence on the evolution of the stress at the point of observation. At t_3 the peak loading pressure level of 16 MPa is attained

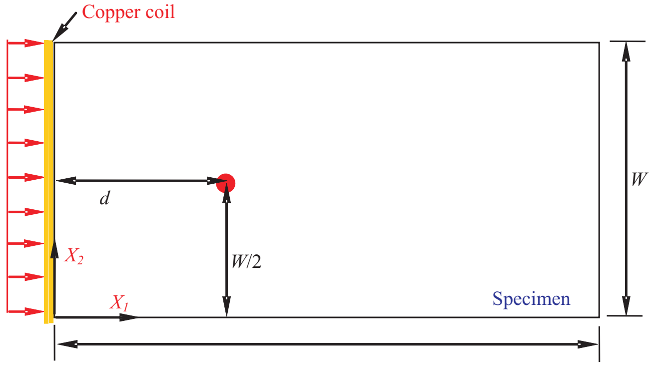

(a)

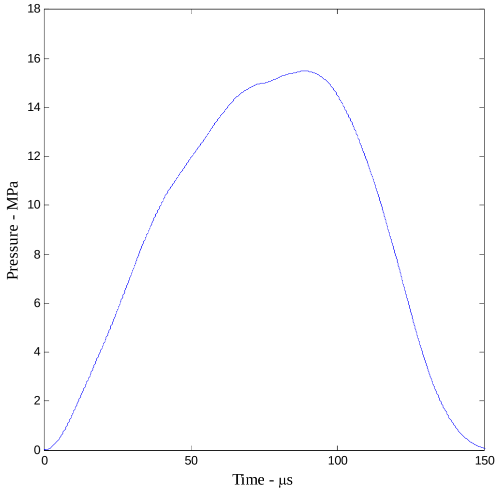

(b)

Figure 5.3: Specimen under uniform dynamic loading. (a) geometry of polycarbonate plate with 230 mm x 114 mm (4.5 x 9 in) and 9.5 mm (3/8 in) thickness. The location of the measurement point is marked by the red circle at $d = 50$ mm; (b) Time variation of pressure loading applied on the edge of the specimen.

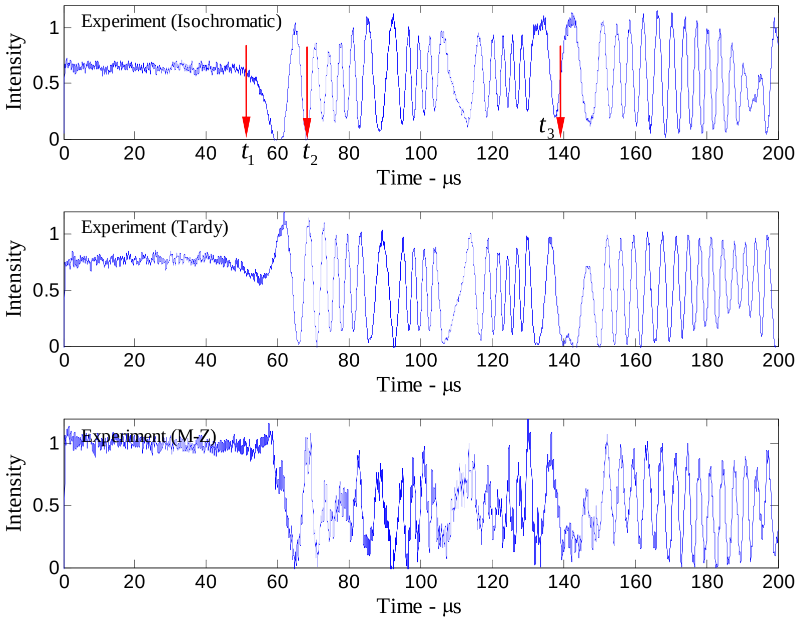

Figure 5.4: Variation of the measured light intensities in the isochromatic, Tardy and Mach-Zehnder arrangements in a Polycarbonate specimen subjected to uniform load.

and hence the fringe number should attain a maximum value at this time. Since the stress begin to diminish beyond this time, the fringe number must decrease. With this interpretation of the fringe data, we can now invert the measured intensities and obtain the stress variation. Before performing this inversion, we will use two independent comparisons, one based on a finite element simulation and another based on direct high speed photography of the isochromatic fringe patterns.

First, the elastodynamic problem was simulated in ABAQUS Explicit (ver 6.6); elastic material properties corresponding to polycarbonate (given in Table 2.1) were used. The pressure pulse corresponding to the experimental measurement (shown in Fig. 5.3 (b)) was applied in the model. The results of the analysis are presented in the following manner: the time variation of the expected light intensities in the isochromatic, Tardy and Mach-Zehnder arrangements was calculated from the numerical simulation using Eqs. (5.1), (5.2) and (5.3) at the point $(d, w/2)$ in the specimen, so that comparisons may be made; the results of these calculations are also shown in Fig. 5.5. Comparing the results in Figs. 5.4 and 5.5, it can be seen that all signals correspond quite well to the measured signals, but with some small discrepancy between the experiment and simulations. We believe that this discrepancy is due to differences between the parameters - loading and material - used in the simulation and the actual experiments (even though this is a simple elastodynamic problem!). To explore this further, the results of the numerical simulation are used to compute the isochromatic fringe patterns (using Eq.

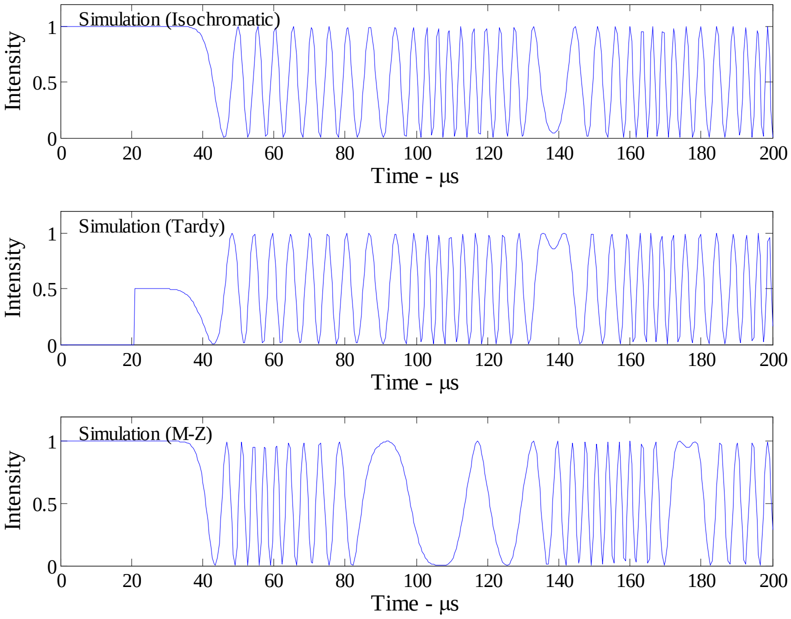

Figure 5.5: Variation of the calculated intensities in the isochromatic, Tardy and Mach-Zehnder arrangements in a Polycarbonate specimen subjected to uniform load.

(5.1)) at fixed time intervals as displayed in Fig. 5.6; these isochromatic patterns are compared to pictures obtained through high speed photography in the same experiment shown in Fig. 5.7. Note that these isochromatics (as well as those from the numerical simulations) correspond to times $143 \sim 220$ μs after impact. While the fringe patterns exhibit qualitative similarity - expected since both correspond nominally to the same material properties, geometrical and loading conditions - there are clearly observable quantitative differences that must be due to the deviations between the idealized pressure loading conditions and material property assumed in the simulations and the actual values in the experimental realization of the problem. The isochromatic data in Fig. 5.7 can be compared quantitatively with the point-wise measurement in Fig. 5.4 by a simple calculation. Consider the isochromatic intensity variation along the center line of frame $\sharp 8$ in the high speed sequence; since the stress field moves to the right as the stress wave propagates, this spatial variation can be considered to arise temporally at the point $(d, w/2)$. Such a comparison is shown in Fig. 5.8; note that only the phase can be compared since the absolute intensity in the high speed photograph depends on various optical elements placed in the optical path. Finally, we present in Fig. 5.9, a comparison of the time variation of the principal stress components determined from the combined isochromatic, isoclinic and Mach-Zehnder intensities to the results of numerical simulations; the principal directions do not change in this one-dimensional problem and are not shown. The applied pressure variation with time is also shown in this figure for comparison. Based on the

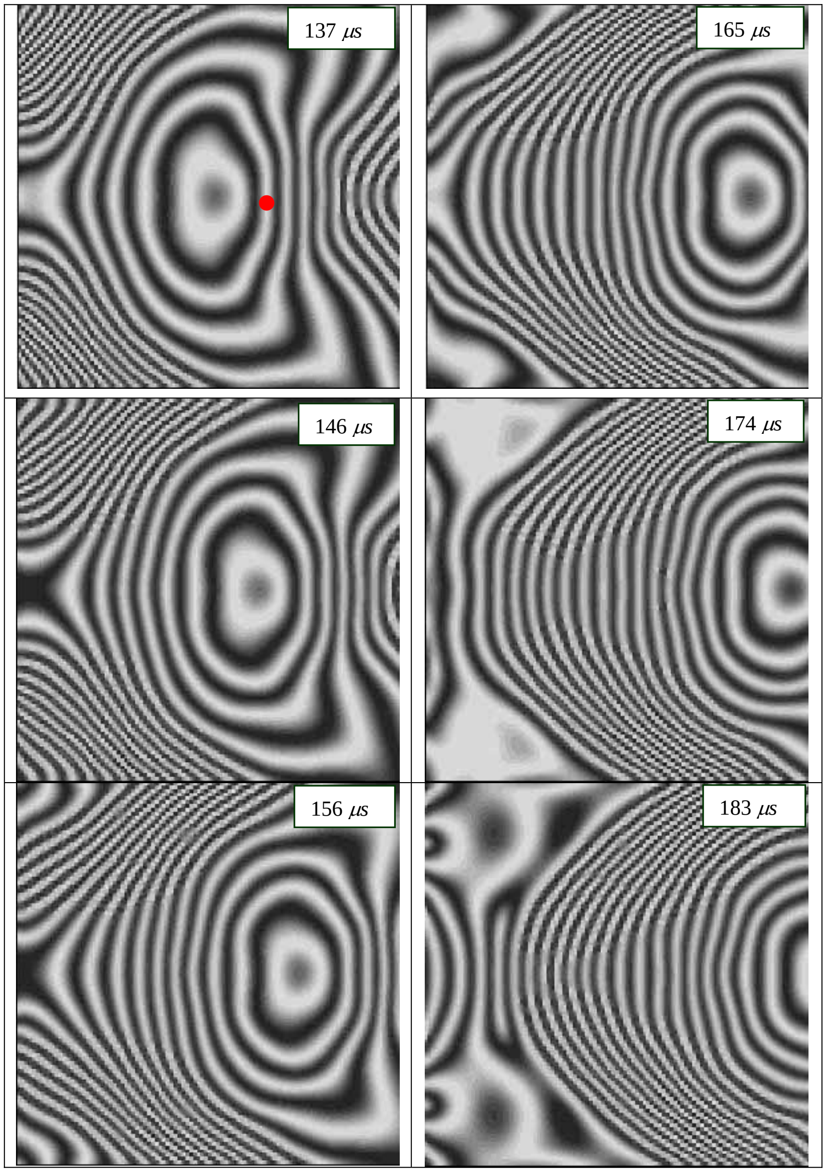

Figure 5.6: Sequence of simulated isochromatic fringe patterns corresponding to a polycarbonate specimen subjected to uniform loading. The red dot marks the location of the point of experimental measurement.

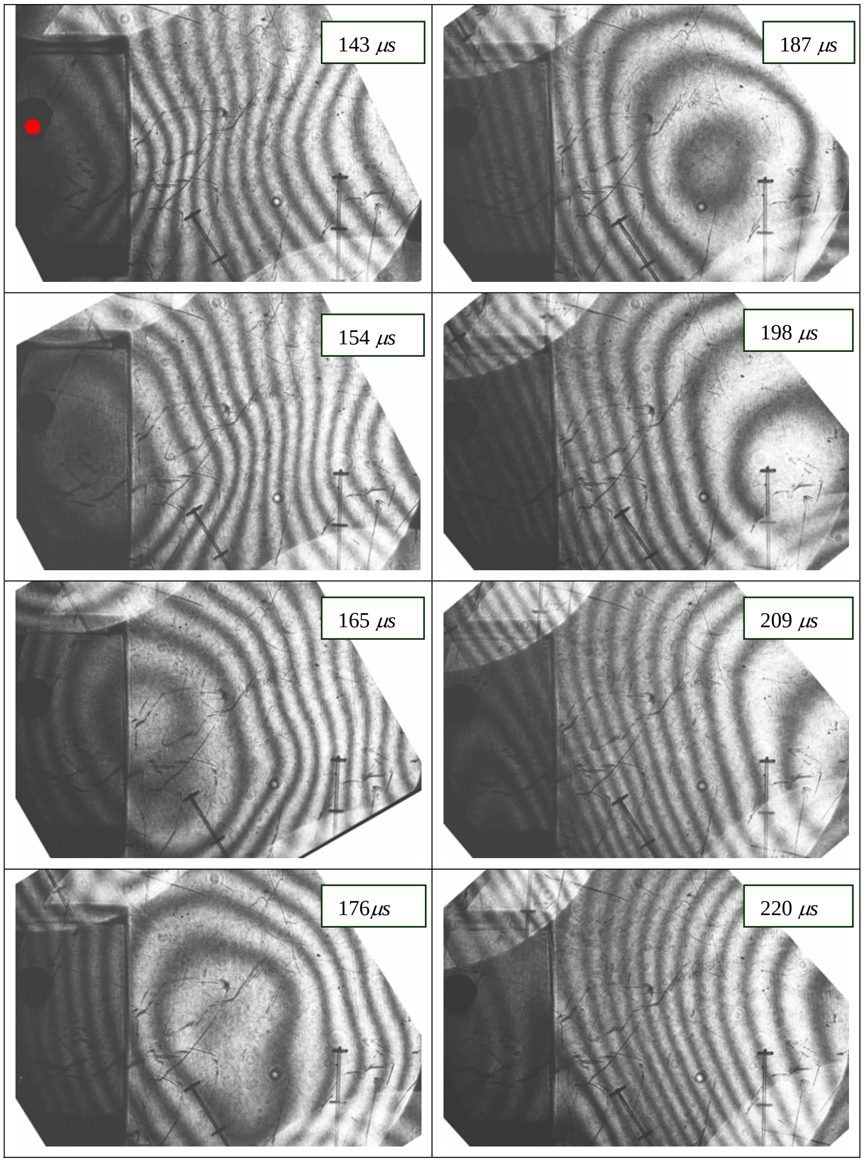

Figure 5.7: Sequence of high speed images showing isochromatic fringes corresponding to a polycarbonate specimen subjected to edge loading. The red dot marks the location of the point of experimental measurement.

excellent correlation between these two measurements, we take the point-wise experimental measurement to be a true indicator of the actual time variation of the stress field at the point of measurement.

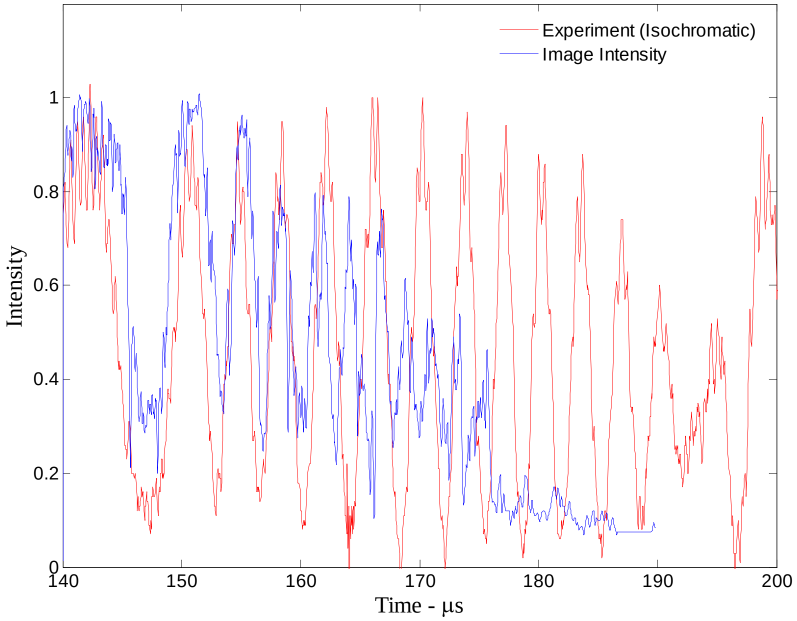

Figure 5.8: Comparison of isochromatic light intensities measured by photodiode and extracted from one high speed image in Fig. 5.7.

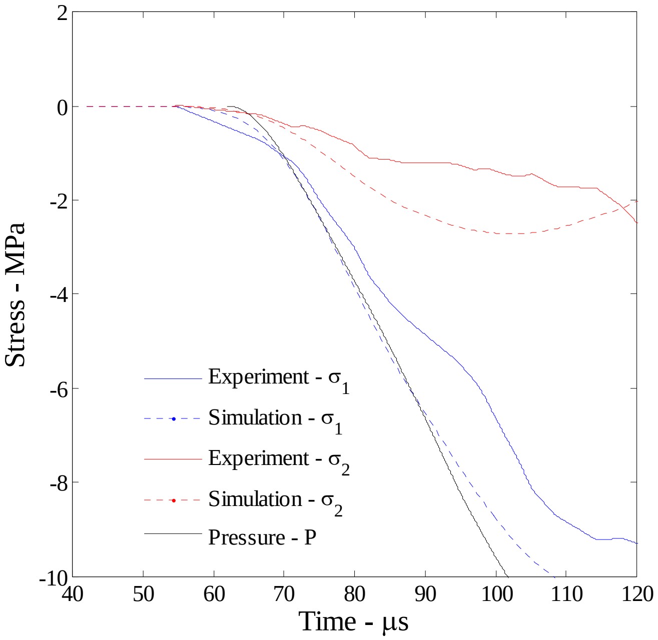

Figure 5.9: Comparison of principal stresses obtained from the experiment with the results of the numerical simulation for the specimen under uniform loading.

Asymmetric Edge loading: We present a second example in order to validate the suggested experimental method. We consider a plate with an asymmetric edge load as illustrated in Fig. 5.10. This arrangement provides a good benchmark for validating the method since the *principal stresses and their orientation change significantly at different points in the specimen.* Two independent measures were adopted for validation of the experiment as described below - a numerical simulation using ABAQUS and a secondary (simultaneous) experimental measurement where the isochromatic fringe patterns over a large region was observed with high speed photography. The time variation of the isochromatic, Tardy and Mach-Zehnder intensities are shown in Fig. 5.11. In this figure, signals from three tests, repeated with nominally the same conditions, are shown in order to demonstrate the repeatability of the measurements. The corresponding quantities estimated from the numerical simulation are shown in Fig. 5.12. The isochromatic patterns from the simulation and from high speed imaging are shown in Figs 5.13 and 5.14 respectively. The main point to note is that unlike in the case of uniaxial loading described in the first experiment, the principal direction does not remain constant and hence the Tardy signal has marked variation in amplitude. The estimates of β from the experiment and numerical simulations are compared in Fig. 5.15. The estimates of the principal stress components from the experiment and simulations are compared in Fig. 5.16. Once again, the comparison is quite good, not only for the principal stress components, but also for the orientation of the principal direction.

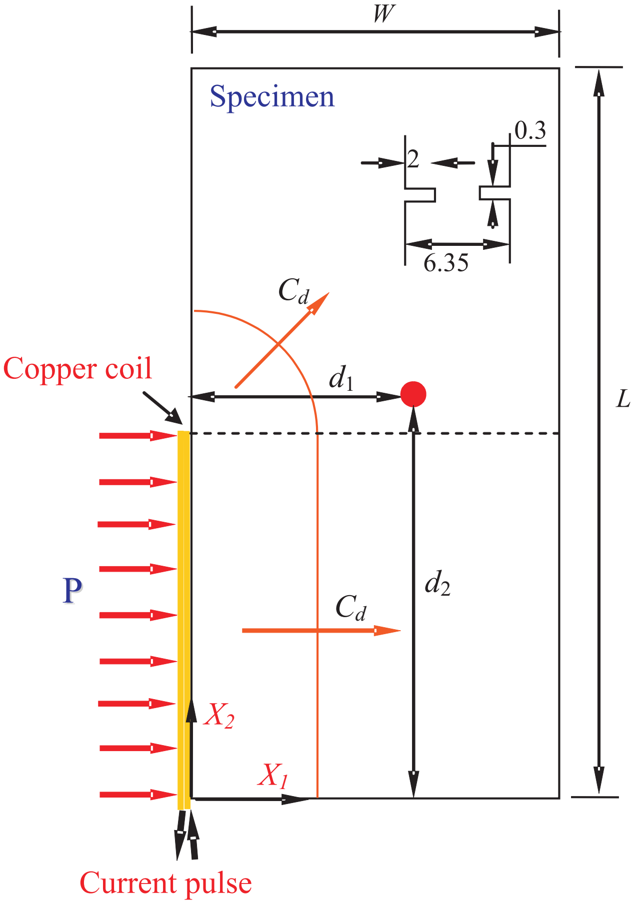

Figure 5.10: Schematic diagram for the specimen under asymmetric edge loading. Polycarbonate plate with a 230 mm x 114 mm (4.5 x 9 in), 9.5 mm (3/8 in) thickness. d_1=70 mm and d_2=120 mm. The red dot marks the location of observation. The dotted line indicates the location of a groove (the details of which are shown inset in the figure). The grooved specimen is used in the third example discussed in this chapter.

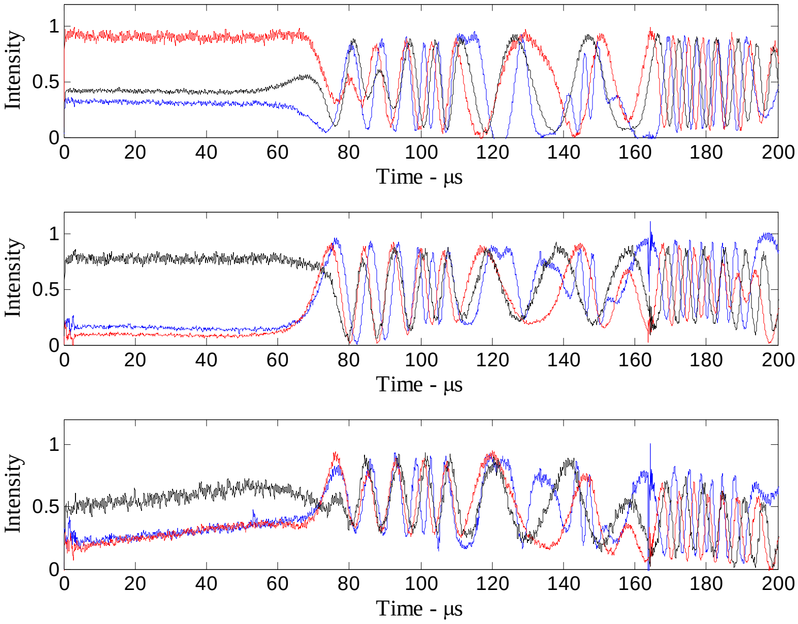

Figure 5.11: Variation of the measured light intensities in the isochromatic, Tardy and Mach-Zehnder arrangements in a Polycarbonate specimen subjected to edge loading; bule, red and black lines indicate test 3, test 4 and test 5 results respectively repeated at nominally the same experimental conditions.

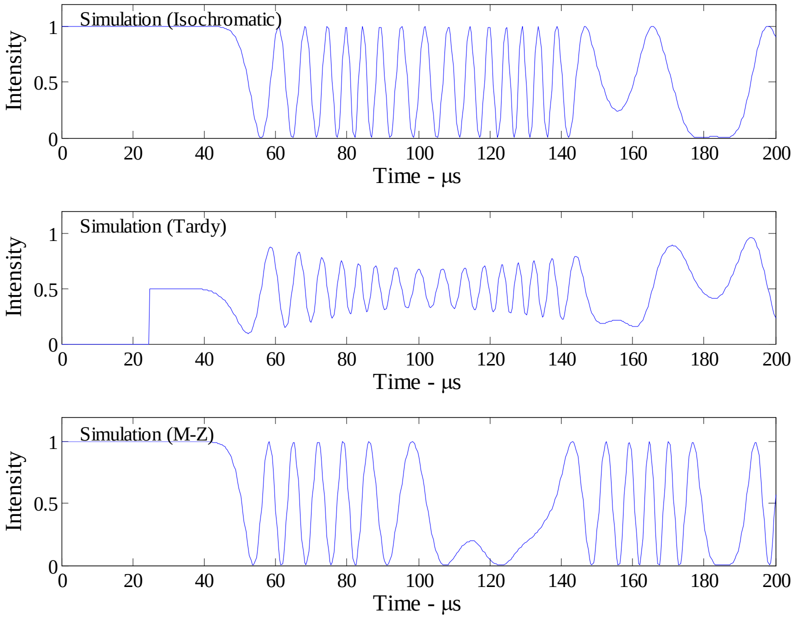

Figure 5.12: Variation of the simulated light intensities in the isochromatic, Tardy and Mach-Zehnder arrangements in a polycarbonate specimen subjected to asymmetric edge loading.

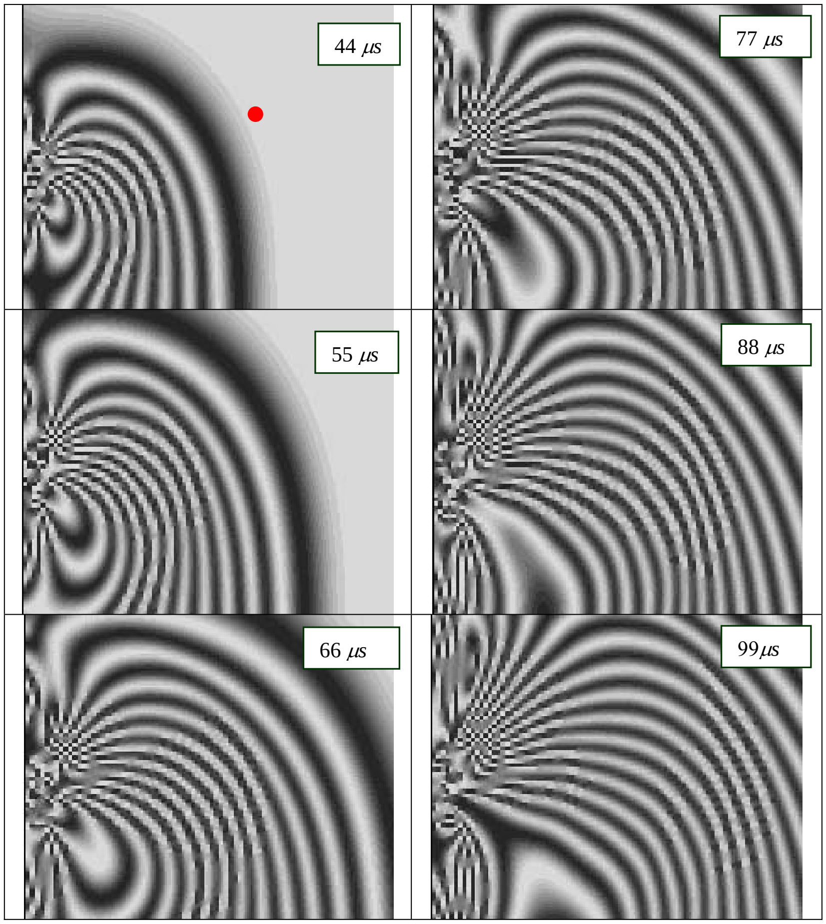

Figure 5.13: Sequence of simulated isochromatic fringe patterns corresponding to a Polycarbonate specimen subjected to edge loading.

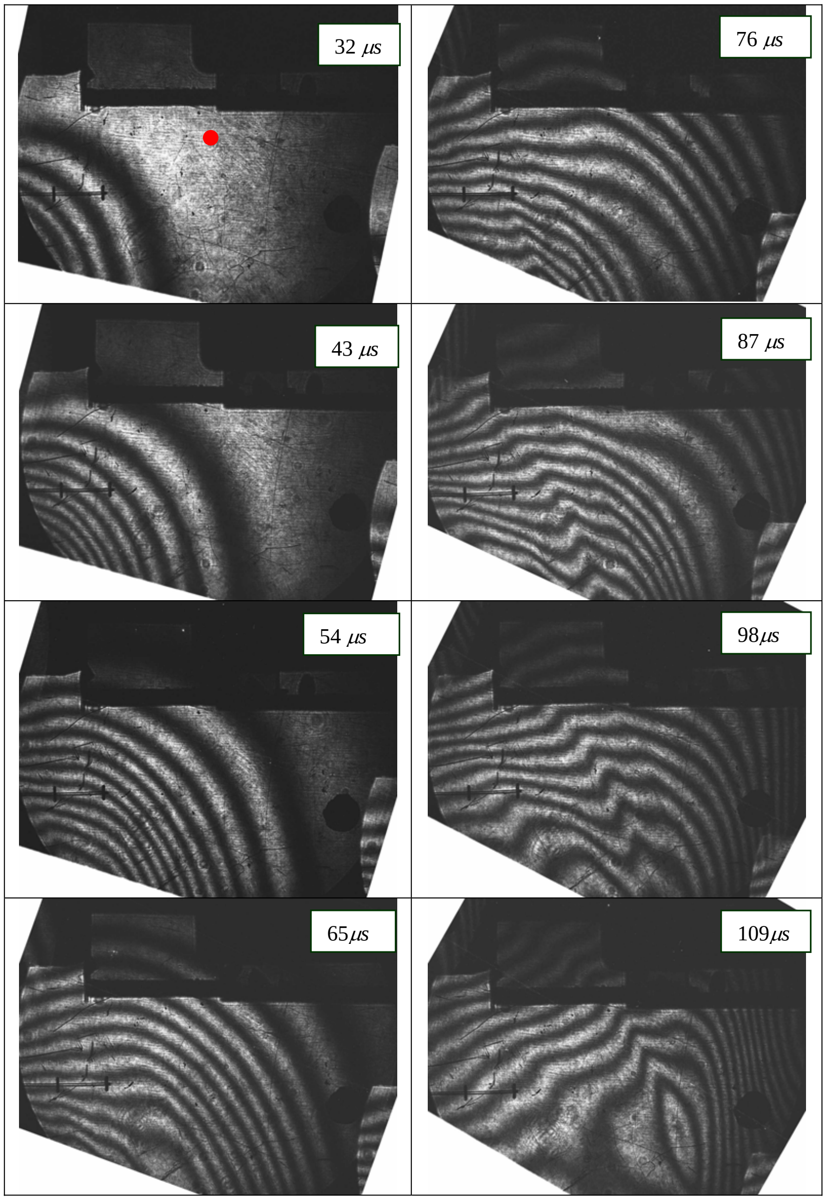

Figure 5.14: Sequence of high speed images showing isochromatic fringes corresponding to a Polycarbonate specimen subjected to edge loading.

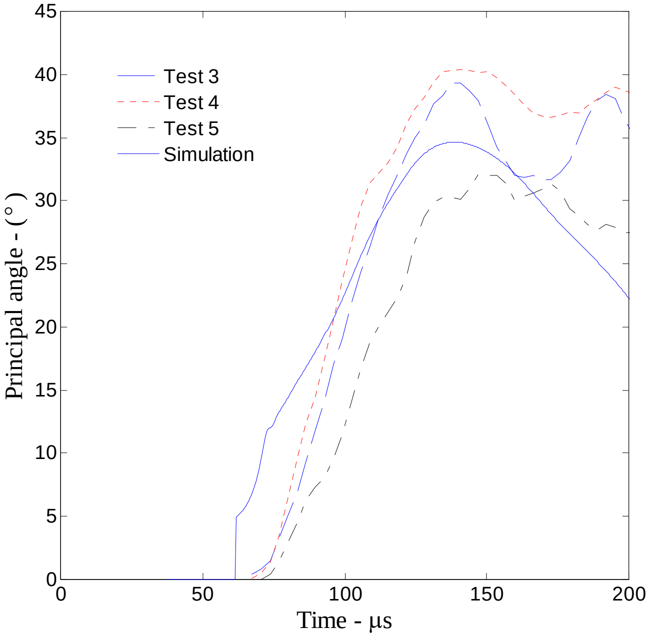

Figure 5.15: Variation of the principal angle with time as determined from the isochromatic and Tardy signals in a polycarbonate specimen subjected to asymmetric edge loading. For comparison, the result from numerical simulations is also shown.

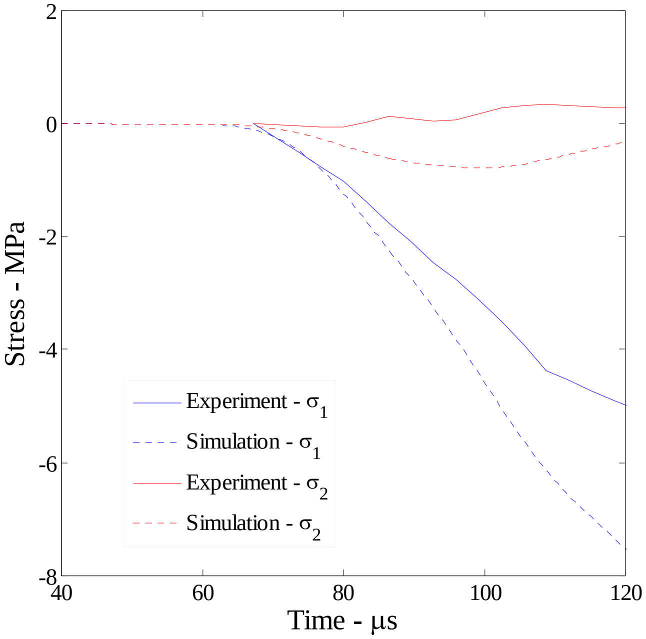

Figure 5.16: Comparison of principal stresses obtained from the experiment with the results of the numerical simulation for the specimen in a polycarbonate specimen subjected to asymmetric edge loading.

Nucleation of Echelon Cracks under Shear Loading: The last example demonstrates an implementation in Homalite-100 that is significantly less sensitive photoelastically. The details of this experiment are described in Section 3.3. This is also an asymmetrically loaded specimen, but with a groove along the direction of impact the details of the groove are shown in the inset sketch in Fig. 5.10. In Section 3.2, we demonstrated the effect of the groove on the stress field of the specimen by using the isochromatic fringe patterns; without changing the global evolution of the stress field, the groove simply serves to concentrate the shear stress within the groove.

Uniform pressure loading with a magnitude of about 45 MPa at 7000 V charge is applied to a Homalite-100 specimen (101.6 mm x 203.2 mm) with the electromagnetic loading device. The compressive stress wave front propagating from the loaded boundary reaches the free end of the specimen (at a distance of 101.6 mm) and returns towards the impact end. As was shown in Section 3.3 this reflected wave interacts with the shear wave from the edge of the asymmetric loading at a location $x_1 = 67$ mm and increases the shear stress significantly from this time. As this stress builds up further, it results in the sequential nucleation and coalescence of echelon cracks, oriented at an angle to the plane of the groove.

In order to determine the state of stress at the time of nucleation of the echelon cracks, we use the stress measurement scheme developed in this work. The isochromatic, Tardy and Mach-Zehnder signals were monitored at the anticipated location (at $x_1 = 67$ mm) of the nucleation of echelon cracks with the point of measurement located just outside the groove; the time variation of these signals is shown in Fig. 5.17. The first signal from the loading arrives at about 50 μs; the interaction between the reflected compression wave and the outgoing shear wave occurs at about 100 μs. For comparison we perform a 3D finite element simulation; in the simulation, the pressure loading (with the peak magnitude of about 45 MPa) calculated from the current measured with the Rogovski coil is applied to a Homalite-100 specimen (101.6 mm x 203.2 mm). The expected light intensities in the isochromatic, Tardy and Mach-Zehnder arrangements from numerical simulations are calculated based on through thickness average of the stresses from the 3D simulation and are compared to the experimental measurements in Fig. 5.17. The measured signal corresponds well to the expected signals until about 100 μs at which time the reflected wave interacts with the incoming shear wave at the position of measurement and crack nucleation and growth along the groove are observed in the experiment. From the experimental signals, the variation of the principal stresses and their orientation are determined as a function of time and are shown in Figs 5.18 and 5.19, respectively; these are compared with the results from ABAQUS simulations in the same figures. The comparison between the simulation and measurement for the stress components is quite good until very close to the onset of echelon cracking; the principle orientation is also reasonably well identified from the measurements. The measured angle between the echelon cracks and the groove plane can be measured directly from the high speed images is approximately 40°. This is somewhat larger than the principal angle variation measured, but this is primarily because the stress state inside the groove where the echelon cracks nucleates is slightly different; the numerical results indicate that the direction of maximum tension inside the groove coincides with the 40° orientation of the echelon cracks.

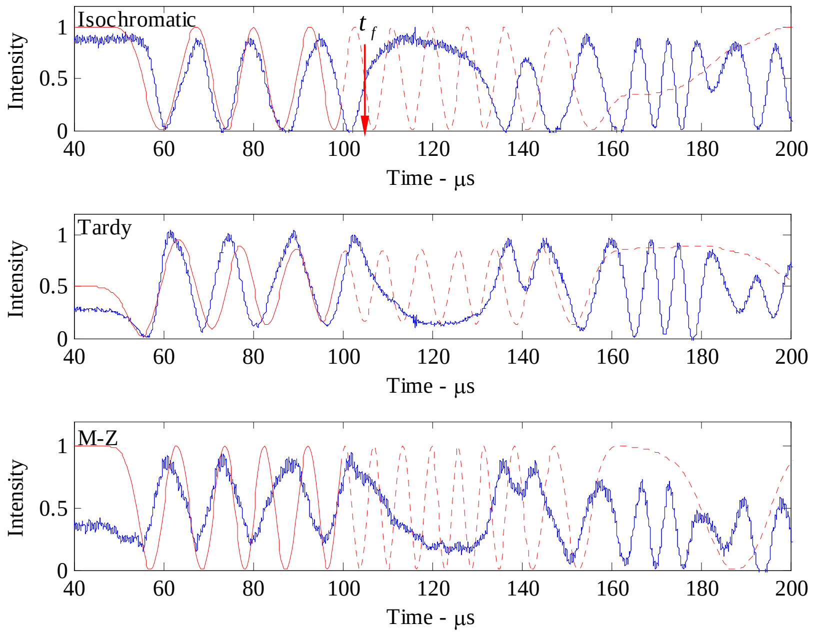

Figure 5.17: Comparison between measured (blue) and simulated (red) variation of light intensities in the isochromatic, Tardy and Mach-Zehnder arrangements in a Homalite specimen subjected to edge loading; The measurement point was located at a distance of 67 mm from the loaded edge, just above the groove line. Since the simulation did not incorporate echelon crack nucleation and growth, the results from the simulation cannot be compared to the experiment beyond about 100 μs and are shown by dotted lines.

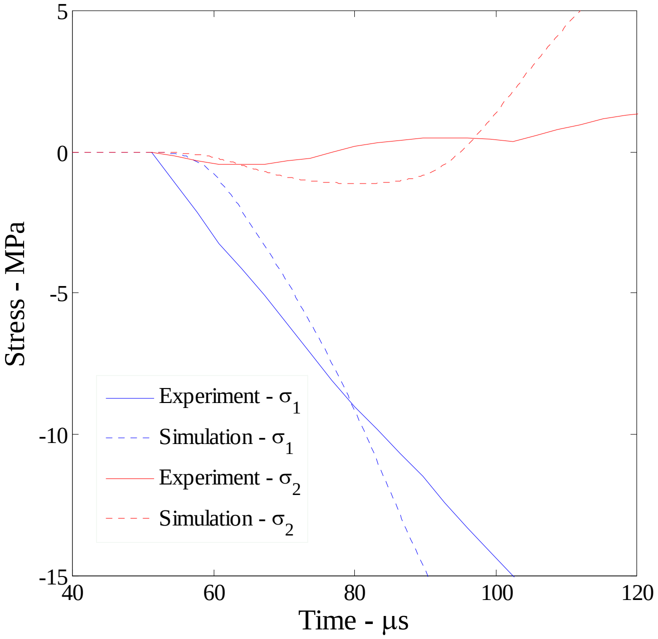

Figure 5.18: Comparison between calculated and simulated principal stress components just above the groove in a Homalite-100 specimen; σ_1 [solid blue line, dashed blue line], σ_2 [solid red line, dashed red line].

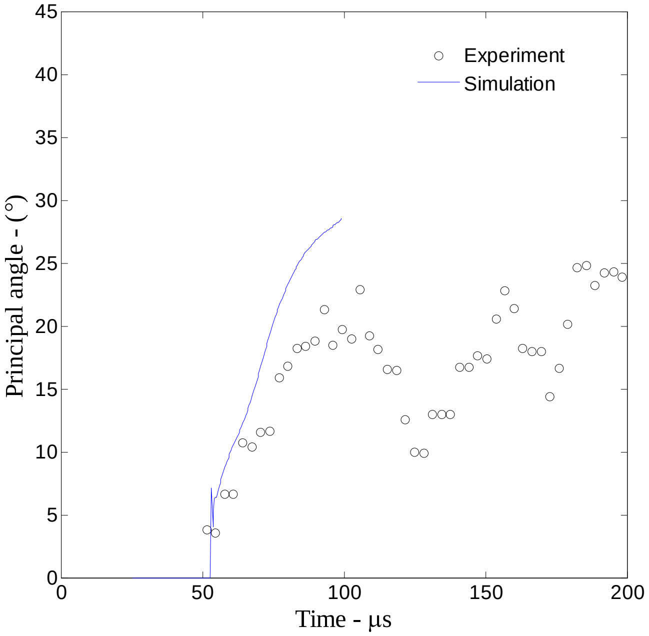

Figure 5.19: Variation of the principal angle with time as calculated from the isochromatic and Tardy signals in a Homalite specimen subjected to asymmetric edge loading. For comparison, the result from numerical simulations is also shown just until the onset of echelon crack nucleation.

In summary, we have adopted classical optical methods of photoelasticity and Mach-Zehnder interferometry in a combined arrangement in order to determine both principal stresses and their orientations simultaneously; high temporal resolution is easily achieved in this arrangement, without the need for high speed photography. In calibration experiments, we validate this method by comparing the measured intensity with the expected intensity and by measuring the variation of the principal angle. This demonstrates that the point-wise experimental measurement is a true indicator of the actual time variation of the stress field at the point of measurement. In a shear crack experiment, the variation of the normal and shear stresses, and the principal stresses and their orientation are determined as a function of time from the measured intensities. We believe that this method will be useful in extracting quantitative stress information in dynamic fracture and friction studies. This method is also easily imposed in quasi-static problems with full-field measurement using multiple imaging cameras.

Chapter 6

Summary and Conclusions

Dynamic fracture and friction under dynamic loading conditions are examined through direct observations in carefully controlled experiments. An electromagnetic loading device is used to generate a compressive stress wave and dynamic photoelasticity and high-speed photography are used for an diagnostic tool as full-field optical techniques. In addition, a new optical method to determine both principal stresses and their orientations simultaneously is presented.

In Chapter 3, dynamic fracture in homogeneous materials under shear loading is presented by introducing a groove in the specimen and trapping the crack to grow within it. This does not affect the fracture mechanisms inherent to the material, but influences the energy flux and loading symmetry. We demonstrate that such shear induced cracks can grow at speeds in the intersonic regime. Furthermore, it is shown that the main mechanism of the shear crack growth is the sequential nucleation, growth and coalescence of echelon cracks. The spacing and angle relative to the groove plane of the echelon cracks are measured directly from the experimental specimen. Numerical simulation shows that the echelon cracks are well aligned perpendicular the maximum principal (tensile) stress generated in this specimen. The spacing is interpreted as an intrinsic characteristic of the failure process. These experiments also enable the determination of the dynamic failure stress at which microcracks are nucleated.

In Chapter 4, frictional sliding has been generated by the interaction of stress waves at the sliding interface. In particular, by orienting the stress wave at an angle to the frictional interface, the projected velocity of the wave along the interface is varied over a large range. The experimental observations indicate that frictional sliding can be driven by such stress waves at the speed of the wave; thus based on stress wave interaction, slip is shown to occur above the dilatational wave speed. The development of the shear stress near the sliding region can be evaluated with the photoelastic fringe patterns, but an additional measurement of the particle velocity is needed in order to obtain characterize the constitutive law for frictional slip. Photomechanics can play a role if digital image correlation or other full field measuring optical technique is used in addition to dynamic photoelasticity.

In Chapter 5, we present the development of a new optical method by adopting classical methods of photoelasticity and Mach-Zehnder interferometry in a combined arrangement in order to determine both principal stresses and their orientations simultaneously. In calibration experiments, we validate this method by comparing the measured intensity with the expected intensity and measuring the variation of the principal angle. This shows that the pointwise experimental measurement is a true indicator of the actual time variation of the stress field at the point of measurement. In shear crack experiments, the variation of the normal and shear stresses, and the principal stresses and their orientation are determined as a function of time from the measured intensities. This method will be useful to extract quantitative stress information in dynamic fracture and friction studies.

Appendix A

Electric Circuit Calibration

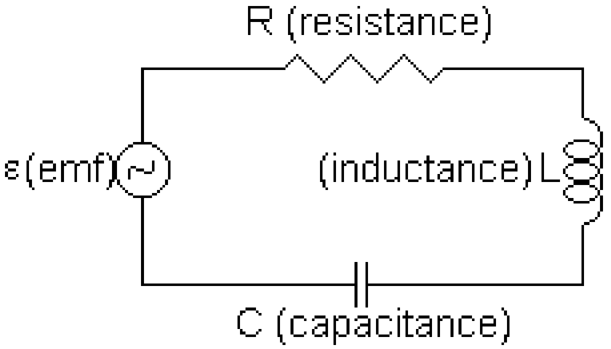

Figure A.1: RLC circuit for calibration of the loading system.

The electromagnetic loading system is equivalent to an RLC circuit shown in Fig. A.1. The current that flows when the ignitron switch is closed is given as:

$$I(t) = -e^{\alpha t} C V_0 \omega [1 + (\frac{\alpha}{\omega})^2] \sin(\omega t) \tag{A.1}$$

$$\alpha = -\frac{R}{2L}, \omega = \frac{2\pi}{T} = \frac{\sqrt{R^2 - 4\frac{L}{C}}}{2L} \tag{A.2}$$

The Rogovski coil is sensitive to $\dot{I}$:

$$\dot{I}(t) = C V_0 (\alpha^2 + \omega^2) \sqrt{1 + (\frac{\alpha}{\omega})^2} e^{\alpha t} \cos(\omega t - \delta) \tag{A.3}$$

$$\delta = \arctan(\frac{\alpha}{\omega}) \tag{A.4}$$

In Eq. (A.4) α can be determined from the ratio of successive peaks of the same sign in the signal shown in Fig. A.2. Finally the current rate at one half period for the calibration shown in the Chapter 3 is calculated as:

$$\dot{I}(t)_{T/2} = -CV_0(\alpha^2 + \omega^2)\sqrt{1 + (\frac{\alpha}{\omega})^2}(\frac{A_3}{A_1})^{\frac{1}{2}} \tag{A.5}$$

A typical current pulse from calibration of the RLC circuit is shown in Fig. A.3.

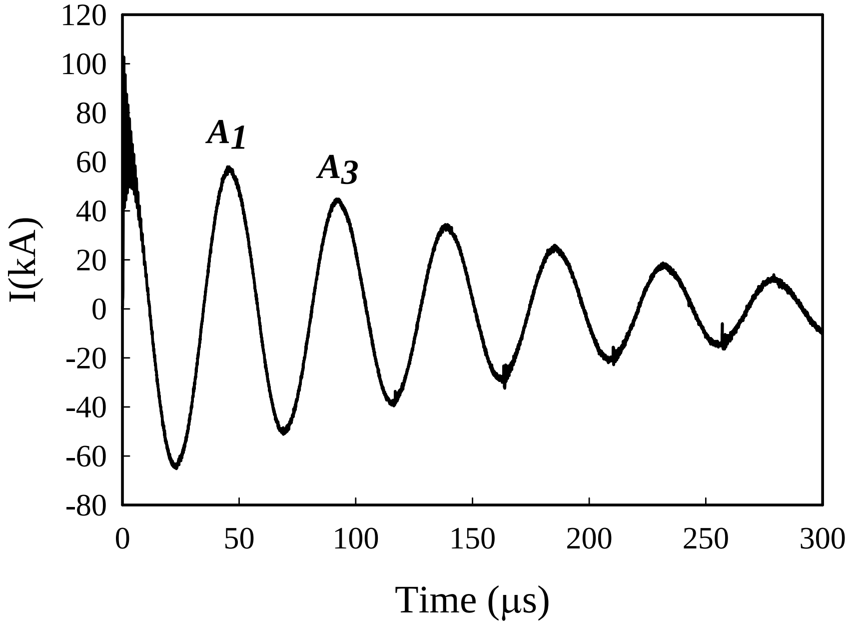

Figure A.2: Current rate signal of the solution to the RLC circuit for calibration ($V_0 = 6000V$).

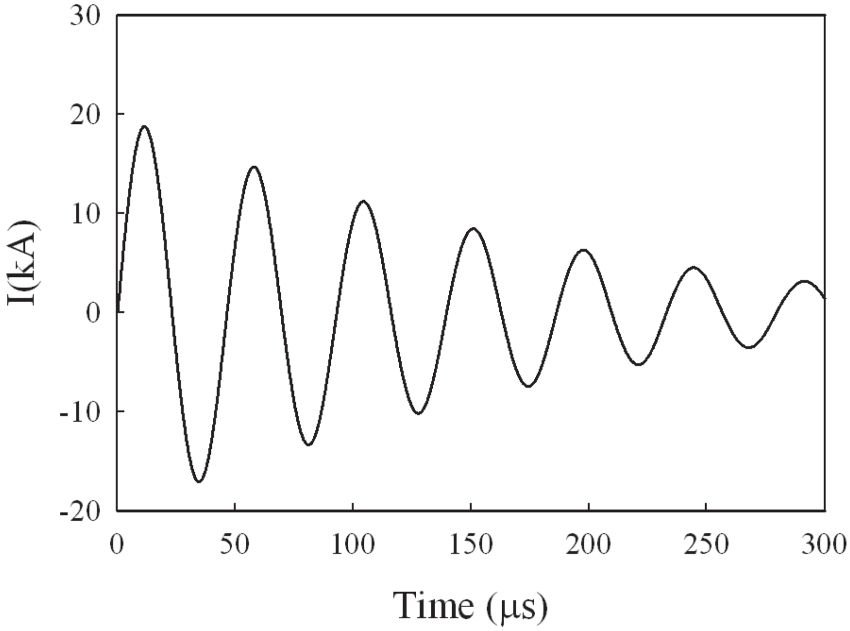

Figure A.3: Current signal of the solution to the RLC circuit for calibration ($V_0 = 6000V$).

Bibliography

[1] G.G. Adams. Steady sliding of two elastic half-spaces with friction reduction due to interface stick-slip. *ASME Journal of Applied Mechanics*, 65:470–475, 1998.

[2] G.G. Adams. An intersonic slip pulse at a frictional interface between dissimilar materials. *ASME Journal of Applied Mechanics*, 68:81–86, 2001.

[3] D.J. Andrews. Rupture velocity of plane strain shear cracks. *Journal of Geophysical Research*, 89:5679–5687, 1976.

[4] R.J. Archuleta. A faulting model for the 1979 imperial valley earthquake. *Journal of Geophysical Research*, 89:4559–4585, 1984.

[5] A. Asundi. Phase shifting photoelasticity. *Experimental Techniques*, 17:19–23, 1993.

[6] D. Brewster. On the affections of light transmitted through crystalized bodies. *Philosophical Transactions*, 104:187–218, 1814.

[7] K.B. Broberg. On crack paths. *Engineering Fracture Mechanics*, 28:663–679, 1987.

[8] K.B. Broberg. The near-tip field at high crack velocities. *International Journal of Fracture*, 39:1–3, 1989.

[9] K.B. Broberg. *Cracks and Fracture.* Academic Press, 1999.

[10] R. Burridge. Admissible speeds for plane-strain self-similar shear cracks with friction but lacking cohesion. *Geophysical Journal of the Royal Astronautical Society*, 35:439–455, 1973.

[11] R. Burridge, G. Conn, and L.B. Freund. The stability of a rapid mode ii shear crack with finite cohesive traction. *Journal of Geophysical Research*, 84:2210–2222, 1979.

[12] Y.J. Chao, P.F. Luo, and J.F. Kalthoff. An experimental study of the deformation fields around a propagating crack tip. *Experimental Mechanics*, 38:79–85, 1998.

[13] M. Comninou, J.R. Barber, and J. Dundurs. Disturbance at a frictional interface caused by a plane elastic pulse. *ASME Journal of Applied Mechanics*, 49:361–365, 1982.

[14] M. Comninou and J. Dundurs. Elastic interface waves involving separation. *ASME Journal of Applied Mechanics*, 44:222–226, 1977.

[15] M. Comninou and J. Dundurs. Elastic interface waves and sliding between two solids. *ASME Journal of Applied Mechanics*, 45:325–330, 1978.

[16] B. Cotterell. Velocity effects in fracture propagation. *Applied Materials Research*, 4:227–232, 1965.

[17] J.W. Craggs. On the propagation of a crack in an elastic-brittle material. *Journal of the Mechanics and Physics of Solids*, 8:66–75, 1960.

[18] J.W Dally. Dynamic photoelastic studies of fracture. *Experimental Mechanics*, 19:349–361, 1979.

[19] J.W. Dally and W.F. Riley. *Experimental Stress Analysis, Third Edition.* McGRAW-HILL, Inc., New York, 1991.

[20] J.H. Dietrich. Time-dependent friction in rocks. *Journal of Geophysical Research*, 77:3690–3697, 1972.

[21] J.S. Epstein, V.A. Deason, and M.G. Abdellah. Phenomenological aspects of bond line and mid-lamina cracks in [0/90]s graphite/epoxy composites under stress wave loading. In *Experimental Techniques in Micromechanics, Vol.102 (W.N.Sharpe, ed). ASME AMD*, San Francisco, USA, 1989.

[22] H. Favre. Sur une nouvelle mthode optique de dtermination des tensions intrieures. *Revue d'Optique*, 8:193–213, 241–261, 289–307, 1929.

[23] L.B. Freund. The mechanics of dynamic shear crack propagation. *Journal of Geophysical Research*, 84:2199–2209, 1979.

[24] L.B. Freund. *Dynamic Fracture Mechanics*. Cambridge University Press, New York, 1990.

[25] L.B. Freund and R.J. Clifton. On the uniqueness of elastodynamic solutions for running cracks. *Journal of Elasticity*, 4:293–300, 1974.

[26] K.F. Graff. *Wave Motion in Elastic Solids*. Dover Publications, New York, 1991.

[27] M.Y. He and J.W. Hutchinson. Kinking of a crack out of an interface. *Journal of Applied Mechanics*, 56:270–278, 1989.

[28] T.H. Heaton. Evidence for and implications of self-healing pulses of slip in earthquake rupture. *Physics of the Earth and Planetary Interiors*, 64:1–20, 1990.

[29] F.W. Hecker and B. Morche. Computer-aided measurement of relative retardations in plane photoelasticity. In *In Experimental Stress Analysis, H.Wieringa (Ed)*, Martinus Nijhoff, Dordrecht, 1986.

[30] M. Kavaturu, A. Shukla, and A.J. Rosakis. Intersonic crack propagation along interfaces: experimental observations and analysis. *Experimental Mechanics*, 38:218–225, 1998.

[31] J. Lambros and A.J. Rosakis. Shear dominated transonic interfacial crack growth in a bimaterial. 1. experimental observations. *Journal of the Mechanics and Physics of Solids*, 43:169–188, 1995.

[32] K.M. Liechti and Y.-S. Chai. Biaxial loading experiments for determining interfacial fracture toughness. *Journal of Applied Mechanics*, 58:680–688, 1991.

[33] J. Lim and K. Ravi-Chandar. Photomechanics in dynamic fracture and friction studies. *Strain*, 43:151–165, 2007.

[34] C. Marone. Laboratory-derived friction laws and their application to seismic faulting. *Annual Review of Earth and Planetary Sciences*, 26:643–696, 1998.

[35] T.W. Ng. Photoelastic stress analysis using an object step loading method. *Experimental Mechanics*, 37:137–141, 1997.

[36] M. Nosonovsky and G.G Adams. Dilatational and shear waves induced by the frictional sliding of two elastic half-spaces. *International Journal of Engineering Science*, 39:1257–1269, 2001.

[37] M. Nosonovsky and G.G Adams. Interaction of elastic dilatational and shear waves with a frictional sliding interface. *ASME Journal of Vibration and Acoustics*, 124:33–39, 2002.

[38] J.T. Oden and J.A.C. Martins. Models and computational methods for dynamic friction phenomena. *Computer Methods-in Applied Mechanics and Engineering*, 52:527–634, 1985.

[39] E.A. Patterson and Z.F. Wang. Towards full field automated photoelastic analysis of complex components. *Strain*, 27:49–56, 1991.

[40] R.D. Pfaff, P.D. Washabaugh, and W.G. Knauss. An interpretation of twyman-green interferograms from static and dynamic fracture experiments. *International Journal of Solids and Structure*, 32:939–956, 1995.

[41] D. Post. Photoelastic evaluation of individual principal stresses by large field absolute retardation measurements. *Proceedings of the Society for Experimental Stress Analysis*, XIII:119–132, 1956.

[42] S. Rajagopalan, M.A. Irfan, and V. Prakash. Novel experimental techniques for investigating time resolved high speed friction. *Wear*, 225-229:1222–1237, 1999.

[43] K. Ramesh. *Digital Photoelasticity - Advanced Techniques and Applications*. Springer-Verlag, New York, 2000.

[44] K. Ranjith and J.R. Rice. Stability of quasi-static slip in a single degree of freedom elastic system with rate and state dependent friction. *Journal of the Mechanics and Physics of Solids*, 47:1207–1218, 1999.

[45] K. Ravi-Chandar. Experiments on dynamic shear crack propagation. In *10th International Conference on Fracture*, Hawaii, USA, March 2001.

[46] K. Ravi-Chandar. *Dynamic Fracture*. Elsevier Inc., San Diego, 2004.

[47] K. Ravi-Chandar and W.G Knauss. Dynamic crack-tip stresses under stress wave loading-a comparison of theory and experiment. *International Journal of Fracture*, 20:209–222, 1982.

[48] K. Ravi-Chandar, B. Lu, J. Yang, and Z. Zhu. Failure mode transitions in polymers under high strain rate loading. *International Journal of Fracture*, 101:33–72, 2000.

[49] A.J. Rosakis. Intersonic shear cracks and fault ruptures. *Advances in Physics*, 51:1189–1257, 2002.

[50] A.J. Rosakis, O. Samudrala, and D. Coker. Cracks faster than the shear wave speed. *Science*, 284:1337–1340, 1999.

[51] A. Ruina. Slip instability and state variable friction laws. *Journal of Geophysical Research*, 88:10359–10370, 1983.

[52] O. Samudrala, Y. Huang, and A.J. Rosakis. Subsonic and intersonic mode ii crack propagation with a rate dependent cohesive zone. *Journal of the Mechanics and Physics of Solids*, 50:1231–1268, 2002.

[53] R.P. Singh, J. Lambros, A. Shukla, and A.J. Rosakis. Investigation of the mechanics of intersonic crack propagation along a bimaterial interface using coherent gradient sensing and photoelasticity. *Proceedings of the Royal Society of London A*, 453:2469–2667, 1997.

[54] A.L. Slepyan, L.I.and Fishkov. The problem of the propagation of a cut at transonic velocity. *Soviet physics Doklady*, 26:1192–1193, 1981.

[55] M.H.L. Tardy. Mthode pratique d'eamen de mesure de la birfringence des verres d'optique. *evue d'Optique*, 8:59–69, 1929.

[56] H.V. Tippur, S. Krishnaswamy, and A.J. Rosakis. Optical mapping of crack tip deformations using the methods of transmission and reflection coherent gradient sensing: a study of crack tip k-dominance. *International Journal of Fracture*, 52:91–117, 1991.

[57] T. Von Karman. Festigkeitsversuche unter allseitigen druck. *Zeitschrift Verein Deutscher Ingenieure*, 118:37–68, 1912.

[58] W.B. Wade and A.S. Kobayashi. An investigation of propagating cracks by dynamic photoelasticity. *Experimental Mechanics*, 10:106–113, 1970.

[59] J. Weertman. Unstable slippage across a fault that separates elastic media of different elastic constants. *Journal of Geophysical Research*, 85:1455–1461, 1980.

[60] A.A. Wells and D. Post. The dynamic stress distribution surrounding a running crack - a photoelastic analysis. *Proceedings of the Society for Experimental Stress Analysis*, 16:69–93, 1958.

[61] T. Wong. Shear fracture of westerly granite from post failure behavior. *Journal of Geophysical Research*, 87:990–1000, 1982.

[62] K. Xia. *Laboratory Investigations of Earthquake Dynamics*. Ph.d. thesis, California Institute of Technology, Pasadena, California, 2005.

[63] K. Xia, A.J. Rosakis, and H. Kanomori. Laboratory earthquakes: The sub-rayleigh-to-supershear rupture transition. *Science*, 303:1859–1861, 2003.

[64] S. Yoneyama, M. Shimizu, J. Gotoh, and M. Takashi. Photoelastic analysis with a single tricolor image. *Optical Lasers Engineering*, 29:423–435, 1998.

[65] J.A Zukas. *Impact Dynamics*. John Wiley and Sons, Inc., New York, 1991.

Vita

Jaeyoung Lim was born in Seoul, South Korea on 26 June 1972. He received the Bachelor of Science degree in the Department of Mechanical Engineering and Design Production from Yonsei University in Korea and was completed military service in Korea Army in 1996. He received the Master degree as a major of the Mechanical Engineering from Yonsei University on February, 2000. He applied to the University of Texas at Austin as a graduate student in their Aerospace Engineering and Engineering Mechanics Ph.D program. He was accepted and started graduate studies in August, 2001.

Permanent address: 7600 Wood Hollow Drive APT 120
Austin, Texas 78731

This dissertation was typeset with LaTeX[†] by the author.

[†] LaTeX is a document preparation system developed by Leslie Lamport as a special version of Donald Knuth's TeX Program.